



## Article

# Impact of the Revisit of Thermal Infrared Remote Sensing Observations on Evapotranspiration Uncertainty—A Sensitivity Study Using AmeriFlux Data

Pierre C. Guillevic <sup>1,2,\*</sup>, Albert Oliso <sup>3</sup> , Simon J. Hook <sup>4</sup>, Joshua B. Fisher <sup>4</sup> ,  
Jean-Pierre Lagouarde <sup>5</sup> and Eric F. Vermote <sup>2</sup>

<sup>1</sup> Department of Geographical Sciences, University of Maryland, College Park, MD 20742, USA

<sup>2</sup> Terrestrial Information Systems Laboratory, NASA Goddard Space Flight Center, Greenbelt, MD 20771, USA; eric.f.vermote@nasa.gov

<sup>3</sup> UMR EMMAH, INRA, Avignon University, 84000 Avignon, France; albert.oliso@inra.fr

<sup>4</sup> Jet Propulsion Laboratory, California Institute of Technology, Pasadena, CA 91109, USA; simon.j.hook@jpl.nasa.gov (S.J.H.); Joshua.B.Fisher@jpl.nasa.gov (J.B.F.)

<sup>5</sup> UMR ISPA, INRA, 33140 Villenave d'Ornon, France; jean-pierre.lagouarde@bordeaux.inra.fr

\* Correspondence: pierreg@umd.edu

Received: 30 December 2018; Accepted: 4 March 2019; Published: 8 March 2019



**Abstract:** Thermal infrared remote sensing observations have been widely used to provide useful information on surface energy and water stress for estimating evapotranspiration (ET). However, the revisit time of current high spatial resolution (<100 m) thermal infrared remote sensing systems, sixteen days for Landsat for example, can be insufficient to reliably derive ET information for water resources management. We used in situ ET measurements from multiple AmeriFlux sites to (1) evaluate different scaling methods that are commonly used to derive daytime ET estimates from time-of-day observations; and (2) quantify the impact of different revisit times on ET estimates at monthly and seasonal time scales. The scaling method based on a constant evaporative ratio between ET and the top-of-atmosphere solar radiation provided slightly better results than methods using the available energy, the surface solar radiation or the potential ET as scaling reference fluxes. On average, revisit time periods of 2, 4, 8 and 16 days resulted in ET uncertainties of 0.37, 0.55, 0.73 and 0.90 mm per day in summer, which represented 13%, 19%, 23% and 31% of the monthly average ET calculated using the one-day revisit dataset. The capability of a system to capture rapid changes in ET was significantly reduced for return periods higher than eight days. The impact of the revisit on ET depended mainly on the land cover type and seasonal climate, and was higher over areas with high ET. We did not observe significant and systematic differences between the impacts of the revisit on monthly ET estimates that are based on morning or afternoon observations. We found that four-day revisit scenarios provided a significant improvement in temporal sampling to monitor surface ET reducing by around 40% the uncertainty of ET products derived from a 16-day revisit system, such as Landsat for instance.

**Keywords:** Evapotranspiration; remote sensing; revisit time period; AmeriFlux

## 1. Introduction

Evapotranspiration (ET) represents the loss of water from the Earth's surface by evaporation of water intercepted by the soil surface and the canopy, and by vegetation transpiration processes. ET has been estimated at about two thirds of the precipitation over land surfaces [1]. Therefore, ET is

a key environmental variable linking the water, carbon, and energy cycles with multiple applications, such as agricultural water management, large scale hydrology, drought monitoring, weather and climate forecasting for example [2,3]. At large scales, ET may be derived by taking advantage of remotely sensed observations of surface variables that are linked to ET. Indeed, ET cannot be directly measured as a flux from satellites, but the response of plants to water and heat stress directly affects the surface energy balance and surface temperature, which can be measured by thermal infrared (TIR) sensors [4–7]. Thermal infrared radiometers at km-scale resolution, such as the Moderate Resolution Imaging Spectroradiometer (MODIS) at 1 km or the Visible Infrared Imaging Radiometer Suite (VIIRS) at 750m resolution, provide daily and spatially continuous information about the land surface temperatures that are commonly used to derive ET and drought indices at large scales [8–11]. However, natural and managed landscapes are usually heterogeneous at smaller spatial scales (<100 m) and require information on biophysical variables at similar spatial scales that can be derived from high spatial resolution observations (<100 m) [12–15]. For water resources management, spaceborne systems must be able to capture rapid changes in land surface temperature (LST) after a precipitation or irrigation event [16] requiring high spatial resolution observations on a frequent basis. However, remote sensing observations are not temporally continuous.

The revisit intervals of current high spatial resolution satellite-based thermal infrared systems (<100 m resolution) are usually insufficient to characterize the energy and water budgets of land surfaces for a variety of research and applications, such as agricultural water resources management. For example, Landsat has a swath width of 185 km and provides global coverage every 16 days, but depending on local cloud coverage, the frequency of clear sky observations is often much lower, limiting its ability to provide data for operational management-appropriate ET estimates [17]. Moreover, optical sensors (from Visible to TIR) require cloud-free observations to derive surface properties; microwave radiometers may provide information about surface temperature in all weather conditions, but at spatial resolutions too coarse for surface heterogeneity detection. To improve the temporal sampling of current TIR observations and ET estimates at high spatial resolution, the NASA ECOSystem Spaceborne Thermal Radiometer Experiment on Space Station (ECOSTRESS) [18–20] was deployed to the International Space Station on 29 June 2018. ECOSTRESS is providing multispectral thermal infrared data to measure the Earth surface temperature at a spatial resolution of  $40 \times 70$  m. The spaceborne system has an average revisit time of four days over 90% of the contiguous United States (CONUS) at varying times of day depending on the latitude [21]. ECOSTRESS will provide a foundation for the proposed Hyperspectral Infrared Imager (HypIRI) mission, with a launch no earlier than 2024 and with a five-day revisit [21]. Other high spatial resolutions and high revisit missions are currently under study. The Copernicus Land Surface Temperature Monitoring (LSTM) mission has been identified as a priority mission by the European Space Agency (ESA) to monitor energy and water budgets and complement the Sentinel program. LSTM has started an ESA preparatory phase study in 2018 to establish mission feasibility. To support agriculture management services, LSTM will have a spatial resolution of 30–50 m and a temporal resolution lower than three days [22]. The French Space Agency (CNES) and the Indian Space Research Organization (ISRO) have also started the design of a new satellite mission called TRISHNA, combining a high spatial resolution (50 m) and high revisit capacities (between two and three days) in the thermal infrared domain [23]. The launch of TRISHNA is planned at the 2024 horizon. Using cloud mask products from MODIS, Mercury et al. [24] found that a five-day revisit period provides a sufficient number of clear-sky scenes to enable both monthly and quarterly surface energy assessments of the vast majority of the Earth's land surface. Using data from a single Landsat satellite (i.e., system with a 16-day revisit period), Allen et al. [17] showed that having at least one cloud-free image per month for selected locations was verified only one year out of the 26-year Landsat archive used by the authors. Using ground station measurements and MODIS cloud masks, Lagouarde et al. [16] estimated that only a one-day revisit spaceborne system could provide on average one cloud-free image every five days over Europe. In a paper focused on future Landsat capacities for water management, Anderson et al. [12] recommend a revisit lower than four

days. Lagouarde et al. [25] pointed out the effect of atmospheric turbulence on surface temperature and recommend revisit periods as high as possible (no value was provided by the authors) to cope with associated LST uncertainties. Alfieri et al. [26] found that a return interval of five days or less was necessary for accurate daily ET estimates, i.e., relative error lower than 20%.

The estimation of daily ET from time-of-day observations is also an existing problem. Current high spatial resolution systems are on sun-synchronous orbits and only provide time-of-day observations which may not be appropriate for water resources management. Therefore, various methods have been developed to scale time-of-day derived ET to daytime or daily averages for management applications [27–29]. A summary of the main temporal scaling methods and key findings is provided in Table 1. The reported methods are based on the assumption of self-preservation of evaporative ratios (ER) between ET and different scaling reference fluxes during daytime [30,31]. Four scaling reference fluxes are usually used: The top-of-canopy (TOC) incoming shortwave radiation (measured or calculated) [32–38], the top-of-atmosphere incoming shortwave radiation [36–39], the surface available energy representing the difference between the surface net radiation and the soil heat flux [4,33,34,36–42], and the surface potential evapotranspiration [35,37,38]. The term “evaporative fraction” (EF) is commonly used when the available energy at the surface is used as reference scaling flux. Prior studies showed that the self-preservation assumption is not verified throughout the daylight hours in general [4,43–45]. Except for the work by Van Niel et al. [36,45], most of the previous studies considered daytime average ET only because the assumption of a constant evaporative ratio is usually not satisfied during nighttime [46]. It should be noted that Kustas et al. [27] and Stannard et al. [47] suggested that the nighttime contribution can represent 5% to 13% of the daytime total depending on vegetation type and soil moisture conditions. Geostationary satellites can provide diurnal information with temporal resolutions from 15 min to 1 h, but the relatively coarse spatial resolution of the thermal bands, e.g., 2 km for the Advanced Baseline Imager (ABI) on the GOES and Himawari series, may cause additional difficulties due to spatial variability of surface biophysical properties within coarser pixels.

In this study, we evaluated the uncertainty on ET retrievals resulting from the scaling of time-of-day measurements up to monthly and seasonal average estimates using ground-based observations made at different AmeriFlux sites spanning a wide range of ecosystems and climates over the contiguous United States. The objective was twofold. First, we compared four different temporal scaling methods commonly used to derive integrated ET over daytime from time-of-day ET retrievals. Then, we evaluated the impact of satellite revisit times on monthly and quarterly ET average. Section 2 presents the different temporal scaling methods that we evaluated, and the methodology used to generate and evaluate the representativeness of the temporal series of monthly and seasonal ET associated with different revisit periods. The AmeriFlux data sets used in the study are described in Section 3, and results are presented and discussed in Sections 4 and 5, respectively. This study was based on in situ ET measurements only and no actual remote sensing observations were used. Therefore, potential errors due to ET retrieval algorithms were not considered, and only uncertainties induced by the scaling and interpolation procedures were evaluated. Throughout the text, specific attention was made on thermal infrared systems because (1) long-term thermal infrared missions at high spatial and temporal resolutions did not exist at the time this article had been published, (2) ECOSTRESS was launched few month ago (June 2018) to demonstrate the need for high spatial and temporal resolutions thermal infrared missions and (3) other thermal infrared missions (i.e., LSTM, TRISHNA) were under study. However, results were based on ground-based direct measurements of ET and were therefore also valid for other systems and spectral domains that could be used to derive ET estimates.

**Table 1.** Summary of techniques used to upscale evapotranspiration from time-of-day observations to daytime or daily scale. Relevant specifications and key findings are also summarized.

Study/Reference	Scaling Quantities <sup>(1)</sup>	Data/Location/Experiment	Relevant Particularities	Key Findings
Jackson et al. [32]	Simulated $R_G$	Crop sites in CA, NE, MN, ID	Daytime scale; impact of cloudiness	Good performance for cloud free days
Brutsaert and Sugita [33]	AE, $R_G$ , $R_n$	FIFE <sup>(2)</sup>	Daytime scale; impact of cloudiness	Good performance of the models based on AE, $R_n$ , $R_g$
Crago [40]	AE	FIFE <sup>(2)</sup>	Daytime scale; impact of cloudiness	Variability of EF depends on cloudiness and advection of moisture
Zhang and Lemeur [34]	AE, Simulated $R_G$	HAPEX-MOBILHY <sup>(3)</sup> experiment	Daytime scale; impact of cloudiness	Constant EF is valid under cloud-free conditions only
Anderson et al. [4]	AE	Large-area implementation	Daytime scale; Used a surface energy balance model	Found systematic error of 10%; Defined correction factor of 1.1
Hoedjes et al. [42]	AE	Olive orchard in Morocco	Daytime scale; Applied correction factor under dry conditions	EF was well preserved under dry conditions only
Van Niel et al. [45]	AE	Two long-term (2001–2008) flux tower sites in Australia	Daily scale; account for observed biases and nighttime fluxes	$\beta$ -correction functions significantly reduce observed bias
Delogu et al. [35]	$R_G$ , PET	Five agricultural fields; three-year datasets	Daytime scale; Interpolation between cloud free conditions	Best performance of the model based on $R_G$ for sites with water stress
Ryu et al. [39]	AE, $R_{TOA}$	34 flux towers from FLUXNET; one-year datasets	Daily scale; No correction factor; Comparison with satellite-based ET	Best performance of the model based on $R_{TOA}$ ; up to 13% bias using AE
Van Niel et al. [36]	AE, $R_G$ (measured and modelled), $R_{TOA}$	Two long-term (2001–2011) flux tower sites in Australia	Daytime scale; $\beta$ -correction factors for each reference scaling flux	Best performance of the model based on $R_G$
Tang et al. [37]	AE, $R_G$ , $R_{TOA}$ , PET	Yucheng, China	Daily scale; All sky conditions	Scaling based on PET had the best performance
Cammalleri et al. [38]	AE, $R_G$ , $R_{TOA}$ , PET	14 Ameriflux sites; two-year datasets	Daytime scale; Applied $\beta$ -correction factor of 1.1 to AE	$R_G$ is the most robust scaling variables; no seasonal variability was found

<sup>(1)</sup> AE: Available Energy, i.e., surface net radiation minus soil heat;  $R_g$ : Surface incoming solar radiation;  $R_{TOA}$ : Top-of-atmosphere incoming solar radiation; PET: Potential evapotranspiration;  $R_n$ : Surface net radiation. <sup>(2)</sup> FIFE: First International Satellite-Land Surface Climatology Project (ISLSCP) Field Experiment. <sup>(3)</sup> HAPEX-MOBILHY: Hydrologic Atmospheric Pilot Experiment, Modélisation du Bilan Hydrique.

## 2. Materials and Methods

The impact of the satellite revisit period on monthly and seasonal ET is evaluated using continuous and long-term ground-based measurements of ET from the AmeriFlux network using the eddy-covariance technique [48].

### 2.1. Scaling ET from Instantaneous Observations to Daytime Averages

#### 2.1.1. Four Scaling Methods Based on Self-Preservation of Evaporative Ratios

In the first part of the paper, we evaluated four different methods commonly used to scale ET from instantaneous observations to daytime averages. The scaling methods are based on daytime self-preservation of the evaporative ratios between ET and different reference scaling fluxes: (1) The top-of-canopy incoming shortwave radiation or solar global radiation ( $R_g$ ), (2) the top-of-atmosphere incoming shortwave radiation ( $R_{TOA}$ ), (3) the surface available energy ( $AE$ ) representing the difference between the surface net radiation and the soil heat flux (measured by the AmeriFlux stations), and (4) the potential evapotranspiration ( $PET$ ).

Daytime evapotranspiration ( $ET_{F,d}$ ) represents the cumulative surface evapotranspiration (in mm) from sunrise to sunset scaled from time-of-day latent heat flux ( $\lambda E_t$ ) using the reference scaling flux  $F$  (Equation (1)).

$$ET_{F,d} = \frac{1}{\lambda} \frac{\lambda E_t}{F_t} F_d, \quad (1)$$

where  $F_t$  is the instantaneous reference scaling flux in  $W m^{-2}$  or joule (J);  $F_d$  is the daytime average scaling flux, i.e., integrated  $F$  over daylight hours from sunrise to sunset in J;  $\lambda$  is the latent heat of vaporization ( $\lambda = 2.45 MJ kg^{-1}$ ). The subscript “ $F$ ” stands for the reference flux used (e.g.,  $ET_{RG,d}$  or  $ET_{AE,d}$ ). Subscripts “ $t$ ” and “ $d$ ” refer to time-of-day and daytime fluxes, respectively. Two of the scaling fluxes ( $R_g$  and  $AE$ ) were directly measured by the stations.  $PET$  was computed using the Penman’s formula [49,50] (Equation (2)) based on measured net radiation ( $R_n$  in  $MJ m^{-2} day^{-1}$ ), wind speed ( $u$  in  $m s^{-1}$ ), air temperature and relative humidity. The Penman’s form of  $PET$  is fully-physically based, including all primary meteorological variables involved in the ET process [51]. It was showed to be the most appropriate form of  $PET$  when considering a changing climate [52], energy-limited environments or ‘equitant’ climate, i.e.,  $PET$  close to the water supply [53]:

$$PET = \frac{\Delta}{\Delta + \gamma} \frac{R_n}{\lambda} + \frac{\gamma}{\Delta + \gamma} \frac{6.43(1 + 0.536 u) VPD}{\lambda}, \quad (2)$$

where  $\Delta$  is the slope of saturation-to-vapor pressure curve depending on air temperature,  $\gamma$  is the psychrometric constant and  $VPD$  is the vapor pressure deficit (in kPa).

$R_{TOA}$  was derived from information on the sun-site geometry only [39]:

$$R_{TOA} = S_{sun} \left[ 1 + 0.033 \cos \left( \frac{2\pi DOY}{365} \right) \right] \cos \theta_s, \quad (3)$$

where  $S_{sun}$  is the solar constant ( $\approx 1360 W m^{-2}$ );  $DOY$  is the day of year;  $\theta_s$  is the sun zenith angle depending on the declination angle, date and location (latitude and longitude) of the sites.

#### 2.1.2. $\beta$ Factors, a Metric to Evaluate the Self-Preservation of Evaporative Ratios

Van Niel et al. [36,45] introduced a  $\beta$  factor ( $\beta_F$  in Equation (4)) to characterize observed biases in the upscaling methods when self-preservation of the evaporative ratio  $\lambda E_t / F_t$  was not verified.  $\beta$  factors were used in this study as a metric to compare and evaluate the four different scaling methods. The  $\beta$  factor is equal to 1 when self-preservation of the evaporative ratio is verified, i.e., the evaporative ratios derived from time-of-day and daytime average fluxes are equal (see Equation (1)).  $\beta$  factors depend on the acquisition time ( $t$ ), land surface type and local climate, and may vary seasonally

due to the non-uniform distribution of precipitation throughout the year and surface hydrology variability. Van Niel et al. [45] calculated  $\beta_{AE}$  factors for the evaporative fraction (i.e.,  $F = AE$  was used as reference scaling flux) and clear-sky conditions only accounting for all available data from two eight-year datasets, while Van Niel et al. [36] accounted for all-sky conditions and average seasonal variability of  $\beta_{AE}$  over two 11-year datasets. Following Van Niel et al. [45],  $\beta$  factors for each site and clear-sky conditions were calculated as the median values of daily  $\beta_{F,i}$  factors over the whole dataset or individual months to account for seasonal variability (Equation (4)):

$$\beta_F = \text{median}(\beta_{F,i})_{i=1, n} \quad \text{with} \quad \beta_{F,i} = \frac{\lambda ET_{d,i}}{F_{d,i}} \frac{F_{t,i}}{\lambda E_{t,i}}, \quad (4)$$

where subscript  $i$  is used to represent the  $i$ -th clear-sky observations in a period of time (month or entire data set in our study) consisting of a total of  $n$  clear-sky observations.

### 2.1.3. Metrics to Evaluate the Different Scaling Methods

Observed discrepancies between the different scaling methods and ground-based average daytime ET were characterized using four different metrics: The  $\beta$  factor (Equation (4)), the median error (ME; Equation (5)), the median absolute deviation (MAD, Equation (6)), and the root mean square error (RMSE; Equation (7)) of the differences.

$$ME = \text{median}(D_{F,i})_{i=1, n} \quad \text{with} \quad D_{F,i} = ET_{F,d,i} - ET_{d,i}, \quad (5)$$

$$MAD = \text{median}\left(\left|D_{F,i} - \text{median}(D_{F,i})_{i=1, n}\right|\right)_{i=1, n}, \quad (6)$$

$$RMSE = \sqrt{\frac{1}{n} \sum_{i=1, n} (D_{F,i})^2}, \quad (7)$$

where  $D_{F,i}$  represents the difference between daytime ET estimated using Equation (1) and measured by a flux tower; the subscripts  $i$  and  $F$  are used to represent individual days in a given set of  $n$  days and the reference flux used for daytime scaling in Equation (1), respectively. In our study, sets of  $n$  days represent the entire data set or sets of days that are either mostly clear or mostly cloudy.

## 2.2. Assessing the Impact of the Satellite Revisit Period on ET

From AmeriFlux data, the study consisted to simulate discontinuous series of ET at a given overpass time (by crossing clear sky conditions with revisit), and then to reconstruct continuous series of daily ET by successively (1) interpolating between successive cloud-free observations and (2) scaling instantaneous observations (as they would be available from space) at daily scale. This study is based on ground data only.

### 2.2.1. Generation of Series of Observations with Different Revisit Periods

The impact of the satellite return period on monthly and seasonal ET estimates was evaluated by comparing different revisit scenarios with two reference datasets: (1) A one-day revisit dataset based on all clear-sky observations made at a given time-of-day by the flux tower, and (2) the daytime average flux tower measurements accounting for all days (including cloudy conditions). The different revisit scenarios are based on the different sampling of clear-sky ground-based observations for a given time-of-day. For each site, an  $n$ -day revisit scenario is derived by selecting the clear-sky observations at the time of the satellite overpass available over the  $n$ -day cycle. As results may depend on the initialization date,  $n$  time series can be derived for each revisit frequency. Then, the  $n$  different samples associated with  $n$  different revisit initializations were compared with the reference datasets and the mean observed discrepancies were used for comparison with other revisit scenarios.



Two overpass times have been considered to represent the nominal times of a morning and afternoon satellite overpass: 10:00 and 13:00. The 10:00 overpass corresponds to instruments like the Thermal Infrared Sensor (TIRS) onboard Landsat-8, the Advanced Spaceborne Thermal Emission and Reflection Radiometer (ASTER), MODIS onboard Terra or the Sea and Land Surface Temperature Radiometer (SLSTR) onboard Sentinel 3, and the afternoon overpass to instruments like MODIS onboard Aqua or VIIRS onboard the Suomi National Polar-Orbiting Partnership (Suomi-NPP) and Joint Polar Satellite System (JPSS) spacecrafts, for example. The afternoon overpass is also the preferred overpass time for missions in preparation, such as TRISHNA or LSTM [22,23]. The impact of acquisition time on the ability to detect water stress and then derive daily ET estimates in accordance with the actual stress level and the stability of temperature measurements was discussed by [54,55]. Lagouarde et al. [55] also showed that the difference between cloud coverage at 10:00 and 13:00 had no significant impact on ET estimates.

### 2.2.2. Interpolation between Clear-Sky Observations

For cloudy conditions or when observations are not available due to satellite return periods, the time-of-day evaporative ratio of the missing day is estimated from consecutive available observations using linear interpolation following the methodology used by Zhang and Lemeur [34]. It should be noted that the linear interpolation does not allow for real time monitoring under cloudy conditions. An example of an eight-day revisit scenario is given in Figure 1, where the TOA incoming solar radiation ( $R_{TOA}$ ) is used to scale time-of-day ET measurements to daytime ET. Eight different eight-day revisit scenarios can be derived from the control one-day series by starting each sample on a different day. The impact of the revisit on ET estimates has been measured using statistical analysis of monthly and seasonal average ET. The four seasonal periods—winter, spring, summer and fall—are December, January and February (DJF); March, April and May (MAM); June, July and August (JJA); and September, October and November (SON), respectively. Two metrics are used to quantify the difference between monthly and seasonal ET average estimated from a given revisit scenario and the ground-based dataset: The root mean square difference/error (RMSE) and a robust estimator of the maximum deviation represented by the median error plus three times the value of the median absolute deviation [56], referred to as maximum deviation estimator hereafter. RMSE is used to characterize the average uncertainty associated with a given revisit period. The estimator of the maximum deviation is used to evaluate the capability of a given revisit dataset to capture short-term changes in surface hydrology, such as the drying period following a moisture event.

### 2.2.3. Clear Sky Identification

In situ measurements made under cloudy conditions were identified based on the departure of the incoming shortwave radiation measured by the station from estimated clear-sky shortwave radiation following [55]. First, for a given location, date and time, the expected value of the clear-sky incoming shortwave radiation is approximated by the maximum value measured by the station over the entire dataset—about ten years of data are available per site on average. Ground-based measurements are flagged cloudy if the measured shortwave radiation is lower than 80% of the estimated clear-sky radiation. On average, the value of 80% represents a good compromise between the need to remove data actually contaminated by clouds and the need to account for possible interannual calibration differences by being overly selective.

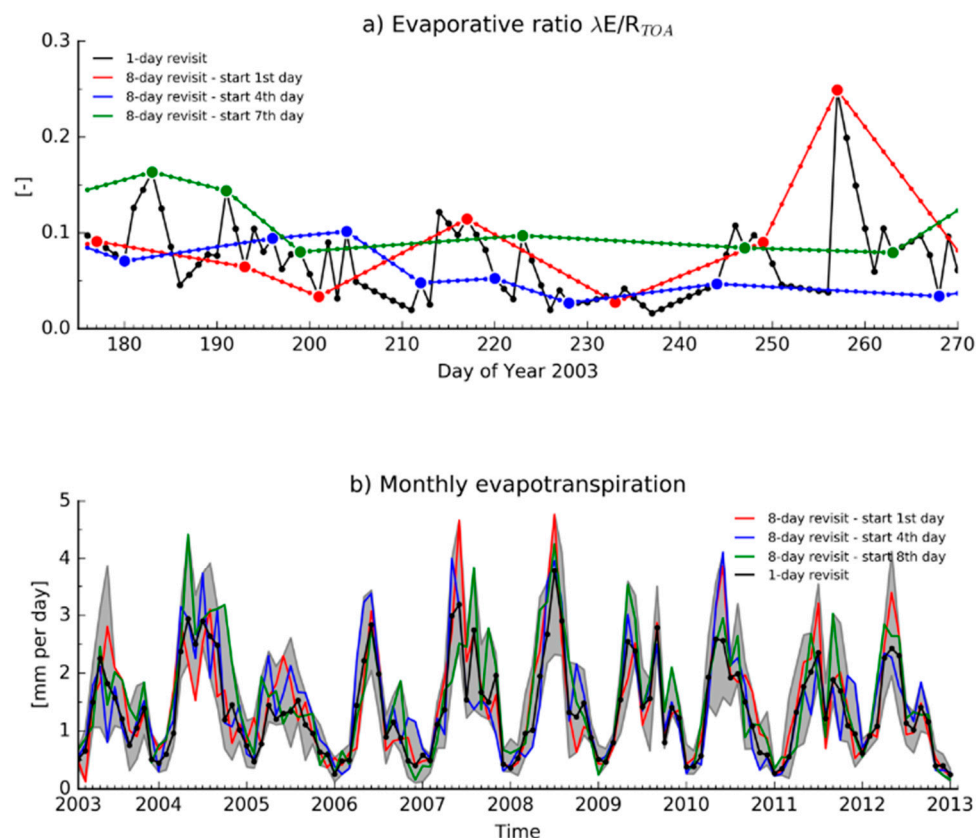


**Figure 1.** Methodology used to generate different revisit scenarios—the figure presents an example of an eight-day revisit scenario using data collected at the Atmospheric Radiation Measurement (ARM) Southern Great Plains, OK. **(a)** A control evaporative ratio series is calculated using ground-based measurements at a given satellite overpass time assuming a one-day revisit period—here the modeled top-of-atmosphere incoming shortwave radiation ( $R_{TOA}$ ) is used as scaling reference flux. Eight different eight-day revisit scenarios can be derived from the control one-day series by starting each sample on a different day. For the eight-day scenarios, the larger markers in **(a)** represent clear sky observations, and the smaller markers represent days with no satellite observations (due to return period or clouds) associated with evaporative ratios estimated from two consecutive clear sky observations using linear interpolation. **(b)** Impact of different eight-day revisits initializations on monthly ET estimates. The gray filled area represents the ensemble of eight-day revisit samples associated with eight different start days.

### 2.3. The AmeriFlux Network

Part of the FLUXNET network [48], AmeriFlux provides continuous observations of ecosystem level exchanges of  $CO_2$ , water and energy, and micrometeorological parameters at diurnal, seasonal, and interannual time scales. We used measurements of radiative forcing (shortwave and longwave downwelling and outgoing radiation), surface fluxes (soil heat and latent heat), and atmospheric parameters (air temperature) collected at 21 AmeriFlux sites over the contiguous United States. The selected stations operate in climatologically diverse regions and are representative of various land cover types (Table 2).



**Table 2.** List of AmeriFlux sites, including site geolocation, primary surface type and period of time considered for each dataset. Ameriflux data availability varies from site to site.

Site	ID	Lat	Lon	Surface Type	Period	Regional Climate	Reference
Southern Great Plains, OK	ARM	36.606	−97.489	Cropland	2003–2012	Temperate	Billesbach et al. [57]
Audubon Ranch, AZ	Aud	31.591	−110.509	Grassland	2004–2008	Semi-arid	Krishnan et al. [58]
Bondville, IL	Bo1	40.006	−88.290	Cropland	1997–2007	Temperate	Meyers and Hollinger [59]
Brookings, SD	Bkg	44.345	−96.836	Grassland	2005–2009	Temperate	Hollinger et al. [60]
Chestnut Ridge, TN	ChR	35.931	−84.332	Deciduous broadleaf	2006–2013	Temperate	Hollinger et al. [60]
Fermi, IL—Agricultural	IB1	41.859	−88.223	Cropland	2006–2011	Temperate	Matamala et al. [61]
Fermi, IL—Prairie	IB2	41.841	−88.241	Grassland	2005–2011	Temperate	Matamala et al. [61]
Fort Peck, MT	Fpe	48.308	−105.102	Grassland	2000–2008	Temperate	Gilmanov et al. [62]
Freeman Ranch, TX—Mesquite	FR2	29.950	−97.996	Grassland	2005–2008	Semi-arid	Heinsch et al. [63]
Freeman Ranch, TX—Woodland	FR3	29.940	−97.990	Woody savannah	2005–2012	Semi-arid	Heinsch et al. [63]
Konza, KS	Kon	39.082	−96.560	Grassland	2007–2012	Temperate	Brunsell et al. [64]
Loblolly Pine, NC	NC2	35.803	−76.668	Evergreen needleleaf	2005–2010	Sub-tropical	Noormets et al. [65]
Loblolly Pine Clearcut, NC	NC1	35.812	−76.712	Evergreen needleleaf	2005–2009	Sub-tropical	Noormets et al. [65]
Mead, NE—Irrigated maize	Ne1	41.165	−96.477	Irrigated cropland	2002–2012	Temperate	Verma et al. [66]
Mead, NE—Irrigated maize-soybean	Ne2	41.165	−96.470	Irrigated cropland	2002–2012	Temperate	Verma et al. [66]
Mead, NE—Rainfed maize-soybean	Ne3	41.180	−96.440	Rainfed cropland	2002–2012	Temperate	Verma et al. [66]
Missouri Ozark, MO	MOz	38.744	−92.200	Deciduous broadleaf	2005–2013	Temperate	Gu et al. [67]
Santa Rita Mesquite, AZ	SRM	31.821	−110.866	Woody savannah	2004–2013	Semi-arid	Scott et al. [68]
Tonzi Ranch, CA	Ton	38.432	−120.966	Woody savannah	2002–2012	Semi-arid	Baldocchi et al. [69]
Vaira Ranch, CA	Var	38.413	−120.951	Grassland	2001–2012	Semi-arid	Ryu et al. [70]
Walker Branch, TN	WBW	35.959	−84.287	Deciduous broadleaf	1995–2006	Temperate	Baldocchi and Meyers [71]

In this study, the primary data set used is the latent heat flux  $\lambda E$  that is derived from eddy-covariance measurements. The footprint of tower-based flux measurements depends on several parameters, such as the sensor height, surface roughness around the tower, wind speed and direction, and atmospheric stability and may vary from a tenth of  $\text{km}^2$  to several  $\text{km}^2$  [72].

AmeriFlux instruments are carefully maintained and a detailed description of the network and a summary of the accuracy assessment of each instrument are provided by Baldocchi et al. [48]. It should be noted that the authors found that quality control tests of surface energy balance closure suggested that turbulent fluxes at some sites are systematically 10% to 30% too small to close the energy budget. Different approaches have been developed to correct for closure issues. They were usually based on the assumption that the convective fluxes are underestimated using the eddy covariance technique [73,74]. Indeed, the non-closure of measured energy balance can be partly due to errors measuring heat storage in the canopy and the upper soil surface layer as mentioned by [75,76], footprint mismatch between the eddy fluxes and the other energy fluxes (net radiation and soil heat) [77,78], inaccuracies in the eddy covariance processing [79], or low frequency turbulence structures not captured by the eddy covariance system [77]. In this study, we did not correct for energy imbalance and used the measured latent heat flux as they were provided in the database. AmeriFlux datasets are archived and distributed by the Oak Ridge National laboratory [80]. For each selected site, the dataset represents 30-min averages of each parameter; the evapotranspiration is represented by the latent heat flux in  $\text{W m}^{-2}$  in the AmeriFlux database.

The selected sites represented four main land cover types: Forests, croplands, grasslands and woody savannahs. We selected locations with companion sites for which the local climate did not vary, but for which the canopy development, plant phenology stage or land water use might differ. Instrumented crops are irrigated or rainfed near Mead in Nebraska; the Loblolly pine stands in North Carolina have different ages: The older stand is around 20 years-old, and the companion site (Loblolly pine clearcut in Table 2) was planted with loblolly pine seedlings in 2004 after a clearcut, for example.

### 3. Results

#### 3.1. Clear Sky Identification

On average over the 21 selected sites, 20 and 19 observations per month were made under clear sky conditions in Summer at 10:00 and 13:00, respectively, around 16 clear-sky observations per month in spring or fall, while only 12 and 14 observations per month were clear in December (Figure 2, one-day revisit period). The median number of clear-sky observations dropped to five and two observations per month for return periods of 4 and 10 days, respectively.

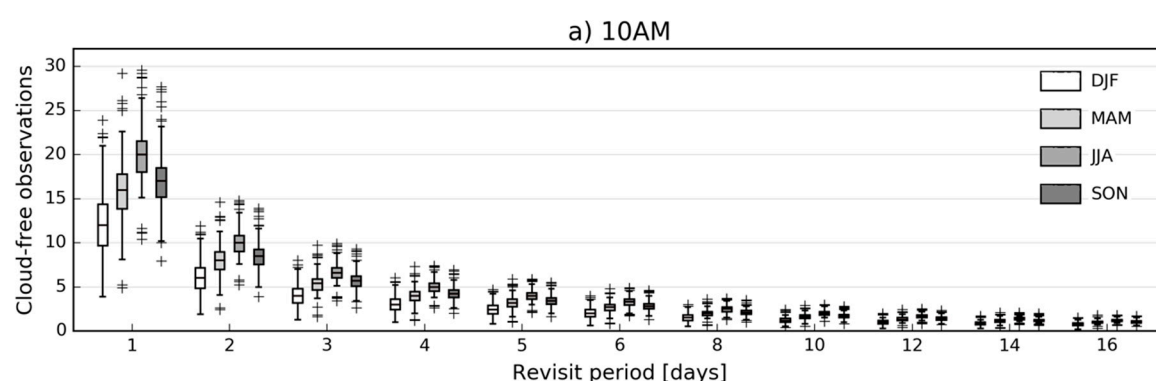
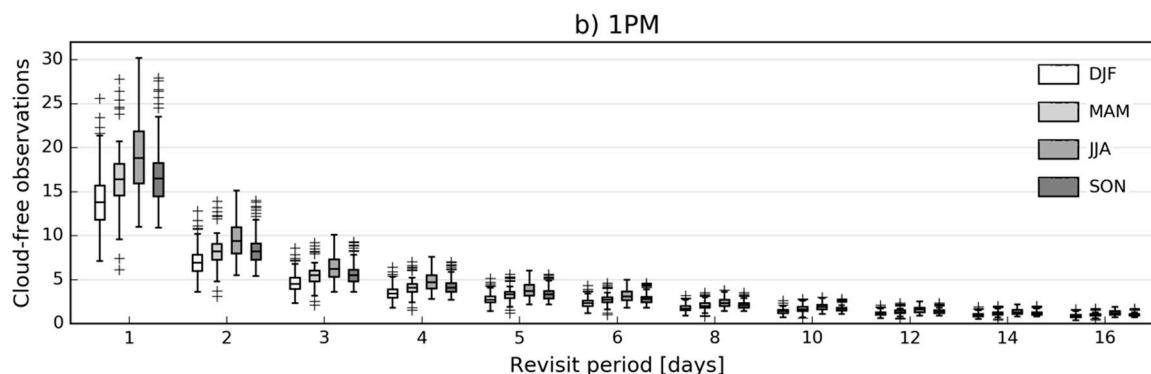


Figure 2. Cont.



**Figure 2.** Number of cloud-free observations per month derived from ground-based incoming shortwave radiation at 10:00 (a) and 13:00 (b) at the 21 flux towers. Average results over all the sites depending on season periods: December, January and February (DJF); March, April and May (MAM); June, July and August (JJA); and September, October and November (SON). The boxes extend from the lower to upper quartile values of the data, with a line at the median. The whiskers represent 1.5 interquartile range below and above the boxes.

However, the impact of cloud coverage may significantly differ from one station location to another (see the spread of data in Figure 2). For example, in July at 10:00, 29 observations were identified clear-sky at Tonzi Ranch, CA on average, but only 16 at Chestnut Ridge, TN. In comparison to the global statistics for cloud-free MODIS observations produced by Lagouarde et al. [23] with a 5 km resolution, we found that ground-based estimates were usually slightly higher than MODIS-derived products. This may be due to differences in spatial scales, i.e., a partly cloudy sky can significantly affect a km-scale satellite pixel and be flagged by the cloud mask algorithm without affecting in situ observations.

### 3.2. Scaling ET from Instantaneous Observations to Daytime Averages

For each site, the multi-year median value and dispersion of the four evaporative ratios ( $\lambda E_t / F_t$  in Equation (1)) were derived from daily clear-sky observations collected at 10:00 and 13:00 (Figure 3; Table A1 in Appendix A), respectively. We also reported (star symbols between the boxplots in Figure 3) the true evaporative ratio based on measured daytime average ET and reference fluxes (i.e.,  $\lambda E T_{F,d} / F_d$ ). As expected, we found lower median evaporative ratios (ER) for sites located in semi-arid areas (Sites referred to as Aud, SRM, Ton, Var in Figure 3). For these sites,  $ER_{AE}$  and  $ER_{TOA}$  varied in the 0.10–0.16 and 0.04–0.1 ranges, respectively. For semi-arid sites, we also observed a higher number of data above the upper whiskers (third quartile + 1.5 interquartile) describing that a relatively low number of precipitation events are associated with high ER values at these sites. We found that time-of-day evaporative ratios based on AE and PET reference fluxes ( $ER_{AE}$  and  $ER_{PET}$ ) usually significantly underestimated the daytime average evaporative ratio and we sometimes observed large differences between ER calculated at 10:00 and 13:00. For example, differences higher than 0.1 in median  $ER_{PET}$  were observed at agricultural sites in Konza (kon) and Mead (Ne1, Ne2, Ne3), for example. Results illustrated the fact that evaporative ratios based on AE and PET were not constant during daytime and might significantly vary with the acquisition time. Such a result has been previously noticed for the evaporative fraction ( $ER_{AE}$ ) in several studies [40,43,44]. Conversely, differences between the two acquisition times (10:00 and 13:00) are usually low for evaporative ratios based on  $R_G$  and  $R_{TOA}$  scaling reference fluxes, suggesting more conservative ratio along the day than for evaporative ratios based on AE and PET.

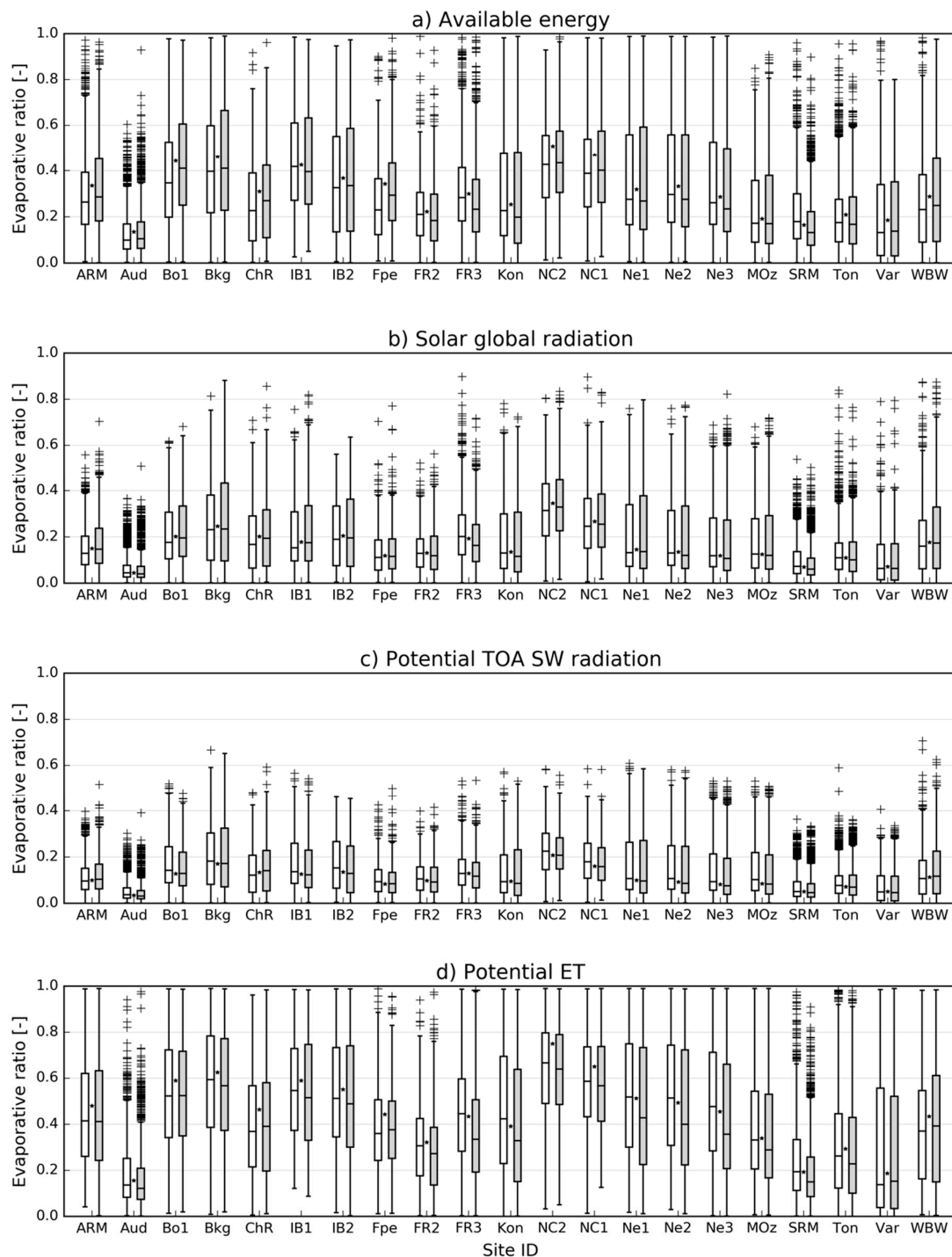


**Figure 3.** Distribution of the evaporative ratios derived for each site and two times of day, 10:00 (white boxes) and 13:00 (gray boxes) based on four different scaling reference fluxes: **(a)** Available energy, **(b)** top-of-canopy incoming shortwave (SW) radiation, **(c)** modelled top-of-atmosphere (TOA) incoming SW radiation, and **(d)** potential ET. The boxes extend from the lower to upper quartile values of the data, with a line at the median. The whiskers represent 1.5 interquartile range below and above the boxes. For each site, the star symbols between boxes represent the median evaporative ratios derived from daytime average ET measured by the station and scaling fluxes. The AmeriFlux site ID labels are defined in Table 2.

Following [36,45], we derived  $\beta$  factors using in situ flux data (Equation (4)) to evaluate the performance of the different scaling methods and verify the assumption of a constant evaporative ratio

during daytime (Figure 4).  $\beta$  factors characterized the bias between estimated and measured daytime ET; they were presented in Figure 4 as a function of the ratio between annual solar radiation measured at the surface ( $R_G$ ) and simulated at the top of the atmosphere ( $R_{TOA}$ ) as a proxy for cloudiness, and the ratio between annual ET and PET as a proxy for aridity [81]. This draws a rough line between temperate (high ET/PET) and semi-arid (low ET/PET) sites. Sites with high (respectively low)  $R_G/R_{TOA}$  ratio were usually associated with lower (respectively higher) ET/PET ratio. The median errors and median absolute deviations between retrieved and measured daytime ET are presented in Figure 5. Results in Figures 4 and 5 were based on clear-sky observations at 13:00 with no restrictions on sky conditions before or after 13:00 (i.e., part of the day could be cloudy). For all scaling methods, we found that  $\beta$  factors tend to increase when the ET/PET ratio decreases or when the  $R_G/R_{TOA}$  ratio increases. For example,  $\beta_{AE}$  factors were around 1.0–1.1 for most of the sites located in temperate regions while varied between 1.2 and 1.3 for sites located in semi-arid regions. Comparing the four scaling methods,  $\beta_{AE}$  factors varied from 1.06 to 1.31,  $\beta_{RG}$  from 0.99 to 1.18,  $\beta_{RTOA}$  from 0.91 to 1.08 and  $\beta_{PET}$  from 1.12 to 1.29 depending on sites (Table A1 in Appendix A). The scaling method based on  $R_{TOA}$  overestimated daytime ET at some of the sites and we found associated  $\beta_{RTOA}$  factors lower than 1 (Figure 4).

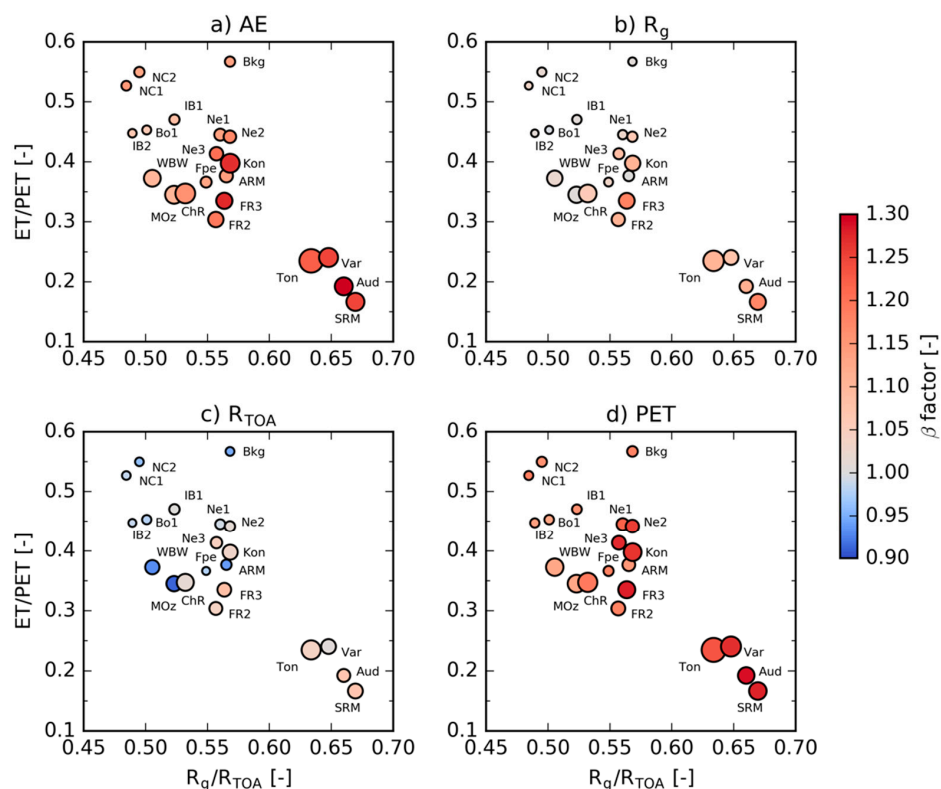


**Figure 4.** All-data  $\beta$  factors (values represented by the colors) derived from observations made at 13:00 for each site depending on the ratio between the annual mean surface solar radiation ( $R_G$ ) and simulated TOA radiation ( $R_{TOA}$ ) and the ratio between the annual mean actual (ET) and potential (PET) evapotranspiration for different reference scaling fluxes: (a) AE, (b)  $R_G$ , (c)  $R_{TOA}$  and (d) PET. The area of the circles represents the median absolute deviation, which varies from 0.09 (smallest circle) to 0.30 (largest circle). The AmeriFlux site ID labels are defined in Table 2.

The dispersion of  $\beta$  factors around the median value was represented by the median absolute deviation (areas of the circles in Figure 4) and tends to increase with a decrease of ET/PET or increase of  $R_G/R_{TOA}$ . The associated median errors (Figure 5) were lower than 0.1 mm per day for the methods based on scaling radiation fluxes ( $R_G$  and  $R_{TOA}$ ). Higher median errors were systematically observed for the methods based on AE and PET, with maximum median errors around 0.2 and 0.3 mm per day, respectively.



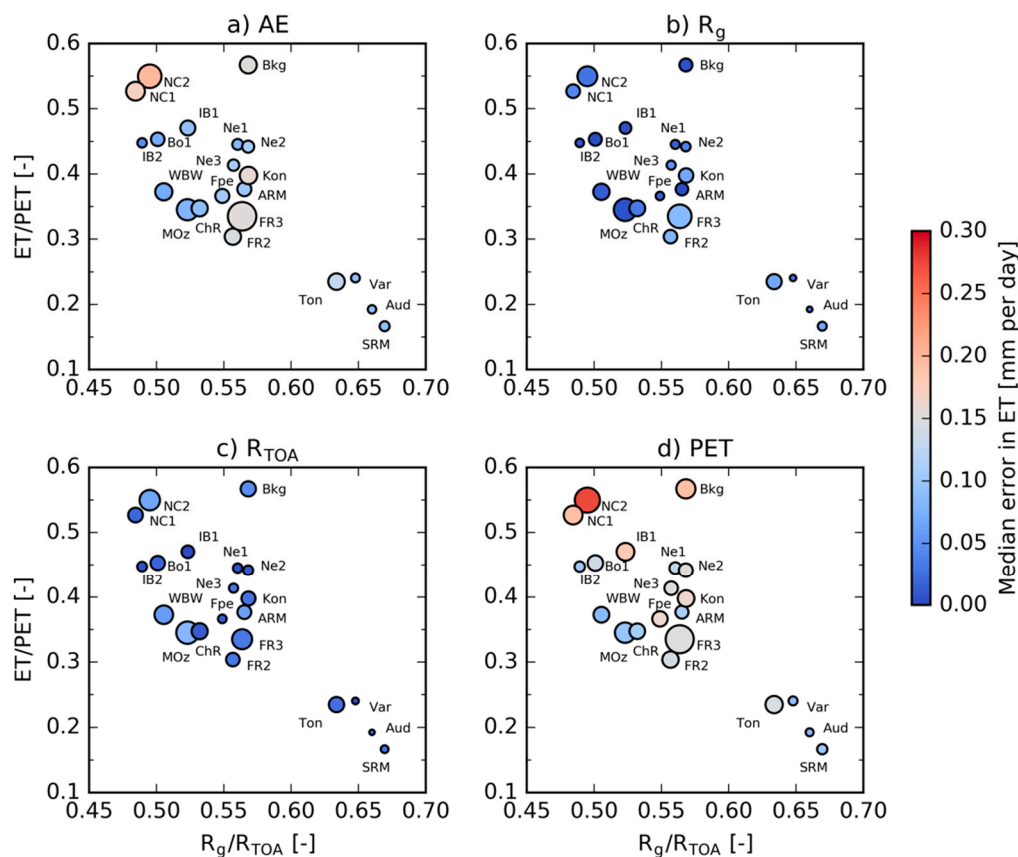


**Figure 5.** Median error (ME, represented by the colors) and median absolute deviation (MAD, represented by the area of the circles) between simulated and measured daytime average ET for each site depending on the ratio between the annual mean surface solar radiation ( $R_g$ ) and simulated TOA radiation ( $R_{TOA}$ ) and the ratio between the annual mean actual (ET) and potential (PET) evapotranspiration for different reference scaling fluxes: (a) AE, (b)  $R_g$ , (c)  $R_{TOA}$  and (d) PET. Scaling to daytime values was based on ET measurements at 13:00 assuming self-preservation between ET and different scaling fluxes. The MAD varies from  $0.06 \text{ mm day}^{-1}$  (smallest circle) to  $0.33 \text{ mm day}^{-1}$  (largest circle). The AmeriFlux site ID labels are defined in Table 2.

Average results derived from all the sites for different sky conditions through daytime before and after clear-sky observations made at two different times (10:00 and 13:00) are presented in Table 3. Daytime periods were considered “mostly clear-sky” when 80% or more of the observations were identified clear. They were considered “cloudy” otherwise. Globally, the scaling method based on simulated  $R_{TOA}$  showed the best performance to scale time-of-day ET observations to daytime average. Accounting for all possible daytime sky conditions (clear and cloudy) before and after clear-sky observations—context of remote sensing applications—and all the sites,  $\beta_{R_{TOA}}$  factor was significantly closer to one than factors derived from other methods: We found  $\beta_{R_{TOA}}$  of 0.93 and 0.99 when based on 10:00 and 13:00 observations, respectively, while  $\beta_{R_g}$  was 1.09 and 1.07,  $\beta_{AE}$  was 1.18 and 1.17 and  $\beta_{PET}$  was 1.11 and 1.20, for 10:00 and 13:00 observations, respectively. As expected, results associated with the  $R_{TOA}$ -based method were slightly better when only clear-sky conditions during daytime were considered, and slightly reduced in quality when only cloudy sky conditions were considered. Median errors of estimated daytime ET based on  $R_{TOA}$  were also lower than those derived from the other methods (Table 3). Differences in median absolute deviations between the methods were relatively small.

Globally, we found that upscaling ET using one of the four selected methods resulted in relatively small median errors (absolute values varying from  $0.01$  to  $0.13 \text{ mm day}^{-1}$  depending on the method used and time-of-day). However, the method based on simulated top-of-atmosphere solar radiation

( $R_{TOA}$ ) slightly outperformed the other methods ( $\beta$  factors closer to one and lower median errors on average) and was used in the next section to evaluate the impact of the revisit period on ET estimates. Also, as already mentioned by [34,39,45], using a simple function to calculate  $R_{TOA}$  and upscale ET to daytime totals represents a viable alternative for large-scale hydrological applications and the use of remote sensing information.

**Table 3.**  $\beta$ -factor (Equation (4)), Median Error (ME) and Median Absolute Deviation (MAD) between simulated and measured daytime ET in mm per day accounting for all the sites. Simulated daytime values were derived from ET measurements at 10:00 and 13:00 and different scaling variables: Available Energy (AE), Observed surface incoming SW radiation ( $R_G$ ), Simulated TOA SW radiation ( $R_{TOA}$ ) and potential evapotranspiration (PET). Results account for clear sky conditions at satellite overpass time and three different sky conditions during daytime: All conditions (clear or cloudy), clear-sky and cloudy-sky conditions.

Sky Condition before and after Clear Overpass	Scaling Flux	10:00 Overpass			13:00 Overpass		
		$\beta$ -Factor	ME	MAD	$\beta$ -Factor	ME	MAD
All conditions (Clear or cloudy)	AE	1.18	−0.12	0.17	1.17	−0.11	0.12
	RG	1.09	−0.06	0.16	1.07	−0.04	0.13
	RTOA	0.93	0.06	0.17	0.99	0.01	0.13
	PET	1.11	−0.08	0.16	1.19	−0.13	0.12
Mostly clear sky	AE	1.18	−0.12	0.17	1.16	−0.1	0.13
	RG	1.07	−0.05	0.15	1.04	−0.03	0.13
	RTOA	0.98	0.02	0.17	1.00	−0.01	0.13
	PET	1.09	−0.06	0.16	1.18	−0.12	0.12
Cloudy sky	AE	1.18	−0.12	0.17	1.18	−0.11	0.13
	RG	1.09	−0.07	0.16	1.07	−0.05	0.13
	RTOA	0.92	0.07	0.18	0.98	0.01	0.15
	PET	1.11	−0.09	0.16	1.20	−0.13	0.13

### 3.3. Impact of the Satellite Revisit Period on ET Estimates

For each land cover type and season, the RMSE calculated between monthly daytime ET derived from the one-day revisit control dataset and the different revisit scenarios increased with the increasing revisit period (Figure 6; Table A2 in Appendix A). For the summer period (JJA), the mean RMSE calculated using the full dataset based on 13:00 observations varied from 0.37 mm per day for a two-day revisit, to 0.55 and 0.73 for a 4-day and 8-day revisit, respectively, and up to 0.90 mm per day for a 16-day revisit scenario (Figure 6; Table A2 in Appendix A). Such differences represented 13%, 19%, 26% and 31% of the average daytime ET derived from the one-day reference sample, respectively. Similar values were obtained for RMSE based on 10:00 observations: From 0.37 mm (13%) to 0.92 mm per day (32%) for the two-day and 16-day revisit scenarios. We found higher RMSE values in summer when the vegetation was fully developed with a maximum of transpiration when soil moisture is not limiting. However, relative RMSE were systematically higher in wintertime, varying from 24% for the two-day scenario to 56% for the 16-day scenario (Figure 6b,d; Table A2 in Appendix A), but associated with relatively low absolute RMSE value (Figure 6a,c). High differences in relative errors values obtained in wintertime were due to low evapotranspiration in winter, which was around 0.4 mm per day on average compared to around 3 mm per day in summer. As a result, small variations in ET had relatively large impacts, but were not really significant. Except for wintertime, no significant differences were observed between results based on the 10:00 and 13:00 datasets when considering all the sites. For a four-day return period (e.g., the temporal resolution of ECOSTRESS), the relative RMSE was around 19% in summer, around 25% during spring and fall and up to 39% in winter. For revisit periods of eight days or more, the relative errors were higher than 33% in spring or fall and up to 45% in wintertime.

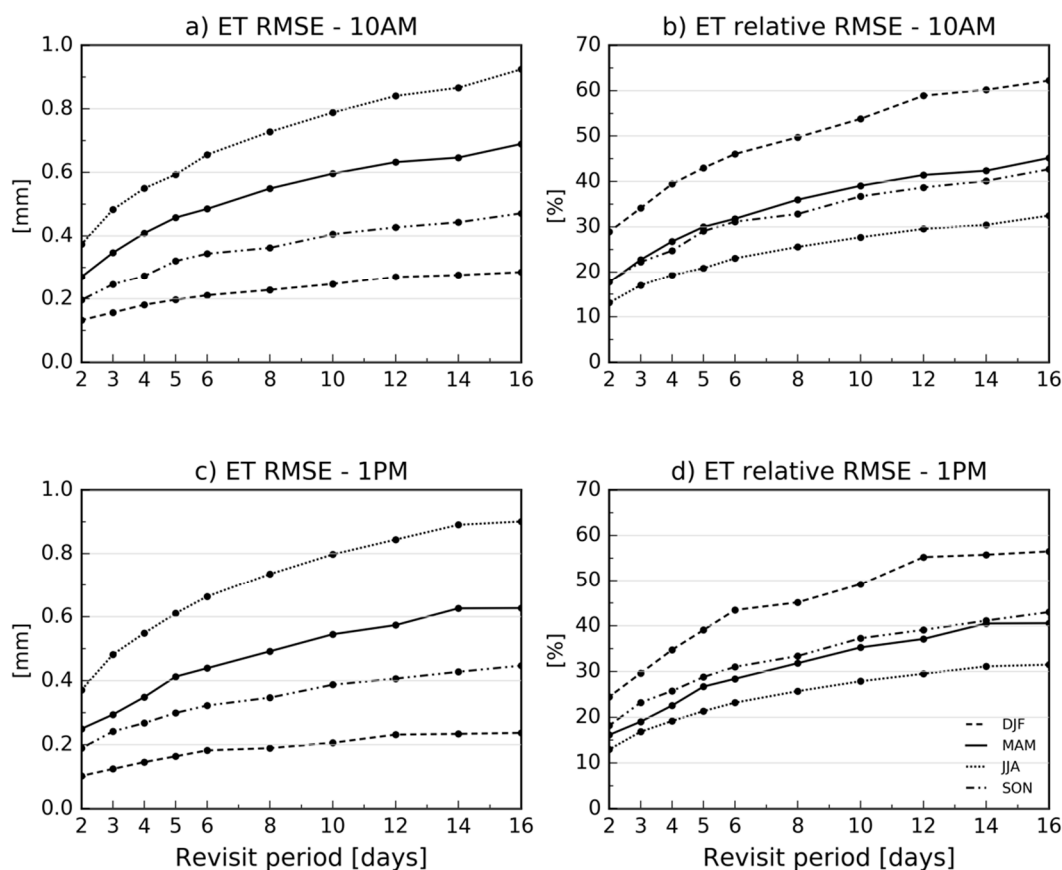


**Figure 6.** Absolute (a,c) and relative (b,d) differences—expressed as Root Mean Square difference (RMSE)—between evapotranspiration (ET) derived from the one-day revisit dataset and derived from the different revisit scenarios for a 10:00 (a,b) and 13:00 (c,d) simulated satellite overpass time. All revisit datasets, including the reference (one-day revisit) were derived from time-of-day clear-sky observations using daytime scaling and interpolation process for the cloudy days. The relative difference represents the ratio between the RMSE and the one-day revisit dataset.

The above results (Figure 6) were obtained when the one-day revisit dataset was selected as the reference dataset to mainly isolate the effect of the satellite return period on ET estimates. The one-day revisit dataset was derived from time-of-day clear-sky observations using daytime scaling and interpolation for the cloudy days. We also calculated uncertainty estimates using the measured monthly daytime ET (integration of all daytime measurements for all sky conditions) as reference dataset (Figure 7) to represent the uncertainties associated with daytime scaling and interpolation processes. The RMSE between the retrieved one-day revisit dataset based on 13:00 observations and the ground-based averages mainly illustrated the uncertainties due to scaling and interpolation processes only, and was 0.08 (18%), 0.22 (15%), 0.33 (12%) and 0.15 (14%) mm per day for winter, spring, summer and fall seasons, respectively. Therefore, observed RMSE between the different revisit scenarios and ground-based measurements were significantly higher than previous results for which the one-day revisit dataset was used as reference: The mean RMSE based on 13:00 observations varied from 0.53 mm per day (19%) for a two-day revisit, to 0.67 (25%) and 0.81 (30%) for a 4-day and 8-day revisit, respectively, and up to 0.94 mm per day (35%) for a 16-day revisit scenario. For water resources management, 30% uncertainty had been reported as the minimum specification of current ET products by [82], and larger uncertainties would be less appropriate for hydrological applications at field scale (~100 m). It should be noted that our results were based on ground-based measurements only and did not account for potential uncertainties of retrieval algorithms when using actual remote sensing data.

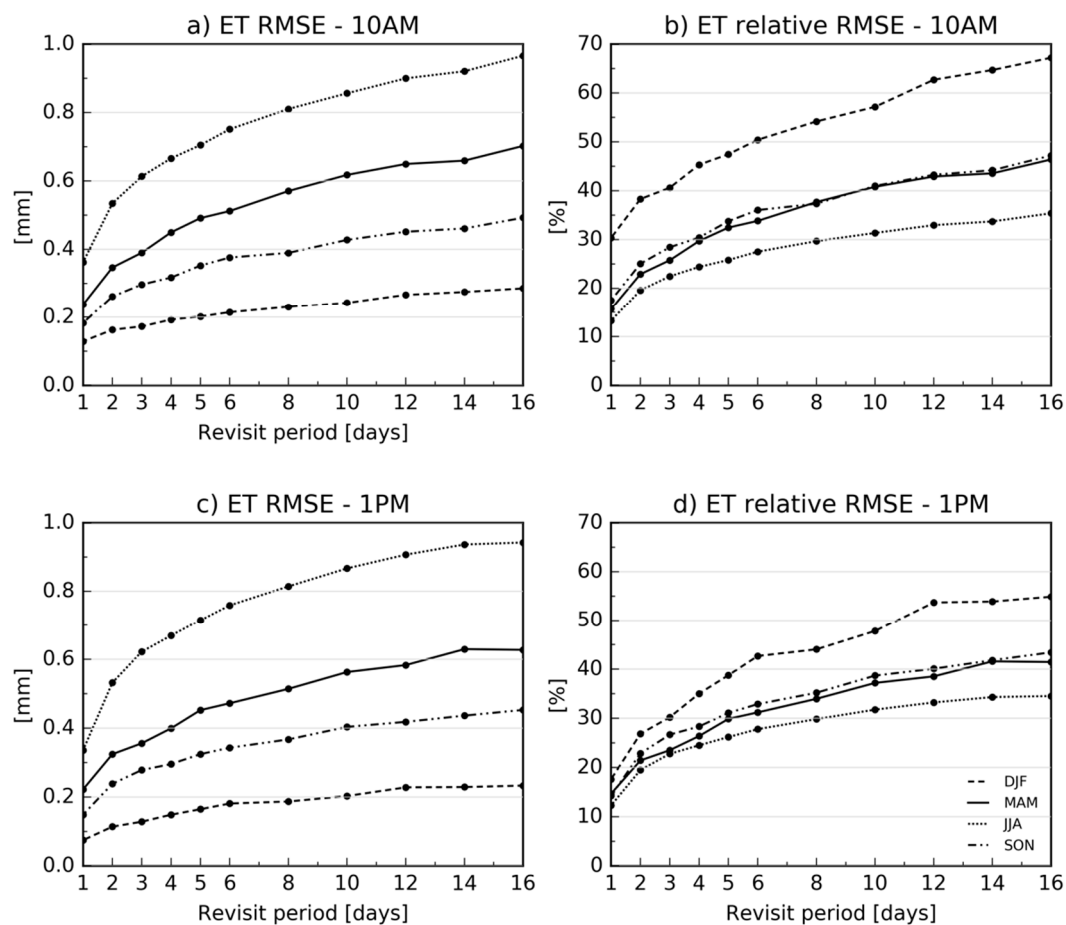


**Figure 7.** Absolute (a,c) and relative (b,d) root Mean Square difference (RMSE) between ET measured by the AmeriFlux sites (integration of all daytime measurements for all sky conditions) and derived from the different revisit scenarios for a 10:00 (a) and 13:00 (b) simulated satellite overpass time using daytime scaling and interpolation process for cloudy days. The relative difference represents the ratio between the RMSE and the measured seasonal mean ET.

The effect of the revisit on ET retrievals depended on multiple factors, such as the land cover type and seasonal climate and was more pronounced for forests and croplands with larger evapotranspiration than woodland savannahs under semi-arid regional climate, for example (Figure 8; Table A2 in Appendix A). Higher uncertainties were observed for forest sites in summer with seasonal RMSE values higher than 1 mm per day for revisit higher than 10 days (at 13:00, Figure 8). For each vegetation biome (i.e., croplands, grasslands, forests and woody savannahs), the return period had a stronger impact in spring and summer and lower impact in winter. However, such an impact of the revisit may vary from year to year depending on climate.

The maximum departure of monthly average ET from the one-day revisit dataset was represented by the maximum deviation estimator (i.e., the median error plus three median absolute deviations) and was used to evaluate the maximum observed uncertainties due to year-to-year climate variability or rapid changes in surface hydrology after particular rain or irrigation events (Figure 9). Accounting for all sites, the maximum deviation estimator of ET using the full dataset based on 13:00 observations during summer (JJA) varied from 0.57 mm per day (33%) for a two-day revisit, to 0.83 (48%) and 1.16 (62%) for a 4-day and 8-day revisit, respectively, and up to 1.43 mm per day (80%) for a 16-day revisit scenario (Figure 9). Similar results were found when using the datasets based on the 10:00 observations. To illustrate both the site-by-site and temporal variabilities, results were disaggregated per site and month of the year in Figure 10. For each site, the observed differences followed a similar seasonal pattern to the monthly average ET. We found higher differences for temperate grasslands and

forests in summer and lower differences for grassland and savannahs in semi-arid regions for which maximum differences due to the revisit were observed during rainy months as expected.

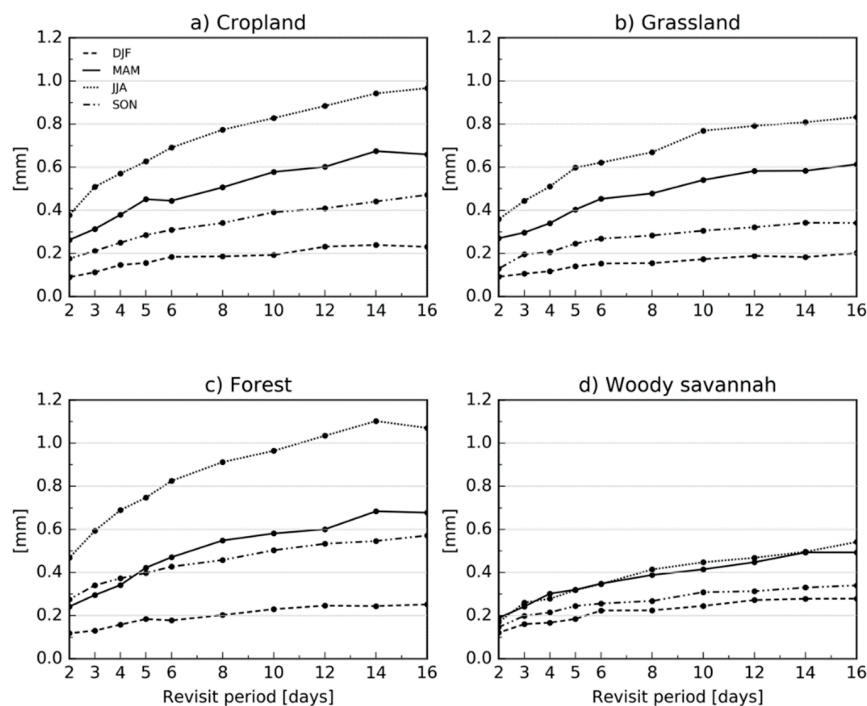


**Figure 8.** Root Mean Square difference (in mm per day) between ET derived from the one-day revisit dataset and derived from the different revisit scenarios for a 13:00 simulated satellite overpass time for different vegetation types: (a) Cropland, (b) grassland, (c) forest and (d) woody savannah.

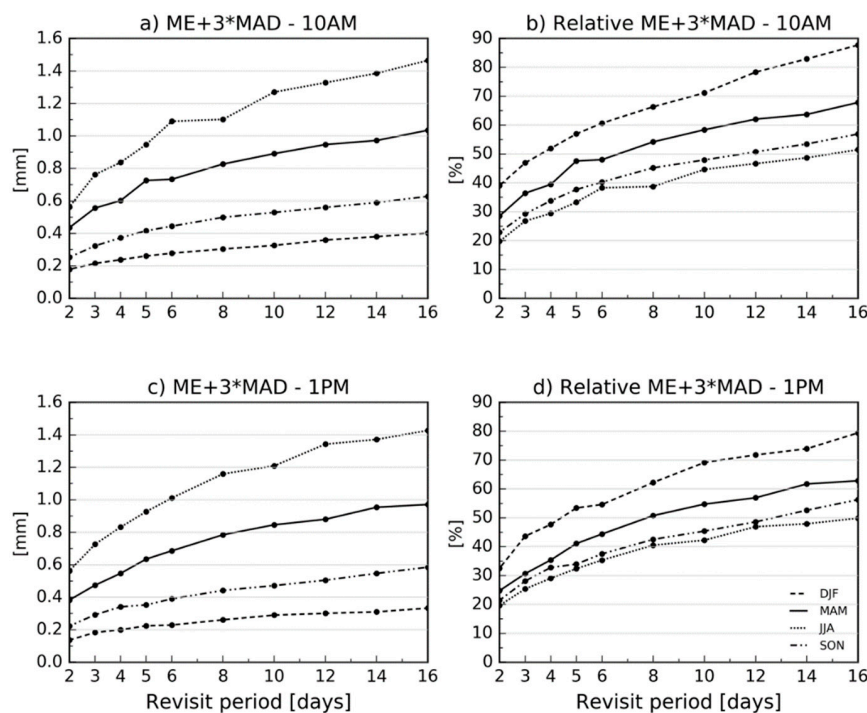


**Figure 9.** Maximum discrepancies (in mm per day)—expressed as the median error (ME) plus three median absolute deviations (MAD)—between the one-day revisit monthly ET dataset and four different revisit scenarios (2-day, 4-day, 8-day and 16-day revisit) for a 10:00 (a,b) and 13:00 (c,d) simulated satellite overpass time. The relative difference represents the ratio between the maximum discrepancy (i.e.,  $ME+3*MAD$ ) and the one-day revisit dataset.



For example, the seasonal variability of monthly average ET of semi-arid grasslands at Audubon Ranch and Vaira Ranch (Figure 10i,j) strongly depended on regional climate, i.e., rainy seasons which were different at those sites. Indeed, at Audubon Ranch, AZ, monthly average precipitation is maximal during July, August and September, but it is minimal and almost nil during those months at Vaira Ranch, CA. As a result, average monthly ET was low, around 2 mm per day at Vaira Ranch in spring and 1.3 mm per day at Audubon Ranch in summer. However, during rainy periods, maximum deviations were relatively large for the 8- and 16-day revisit and around 65% of the monthly mean for particular months at Audubon Ranch. Such differences were most likely due to rain events followed by periods of higher evapotranspiration that were not or only partly captured by the sampling, but that significantly modified the surface hydrology and monthly means. The observed differences for semi-arid sites were higher for ET estimates based on observations made at 13:00 than 10:00, probably due to the effect of water stress that is usually prevailing in the afternoon. No significant differences between results based on 10:00 or 13:00 measurements were found for the other sites. In general, only the two-day revisit datasets provided maximum deviations from the one-day revisit lower than 1 mm per day throughout the year.

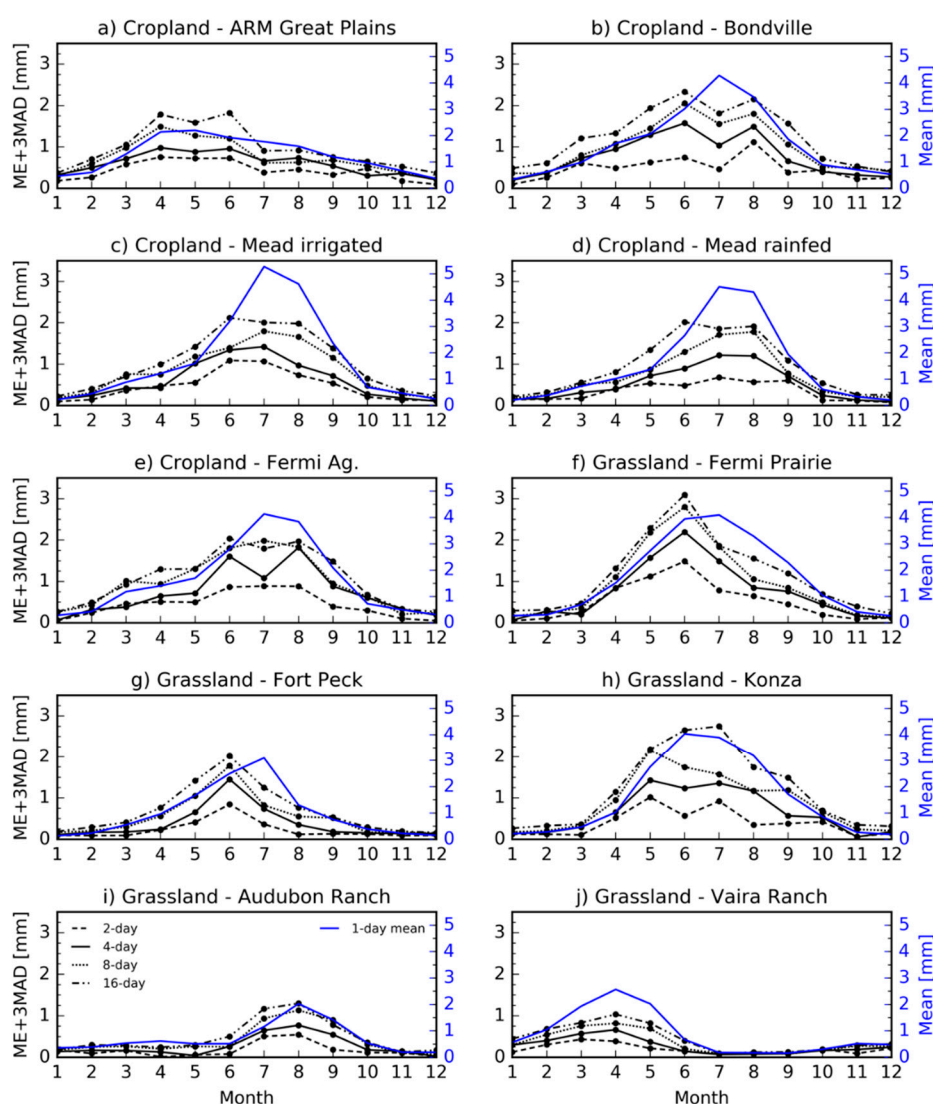
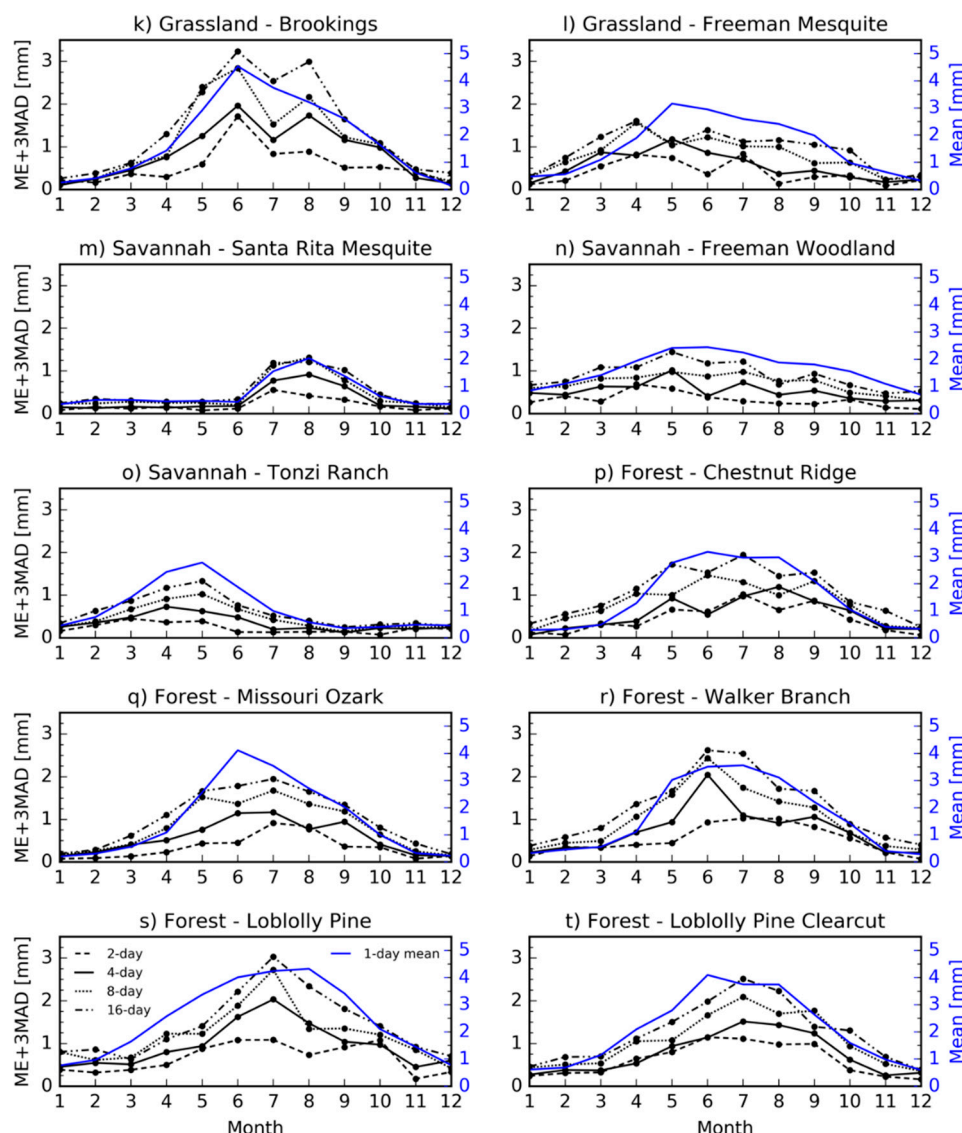
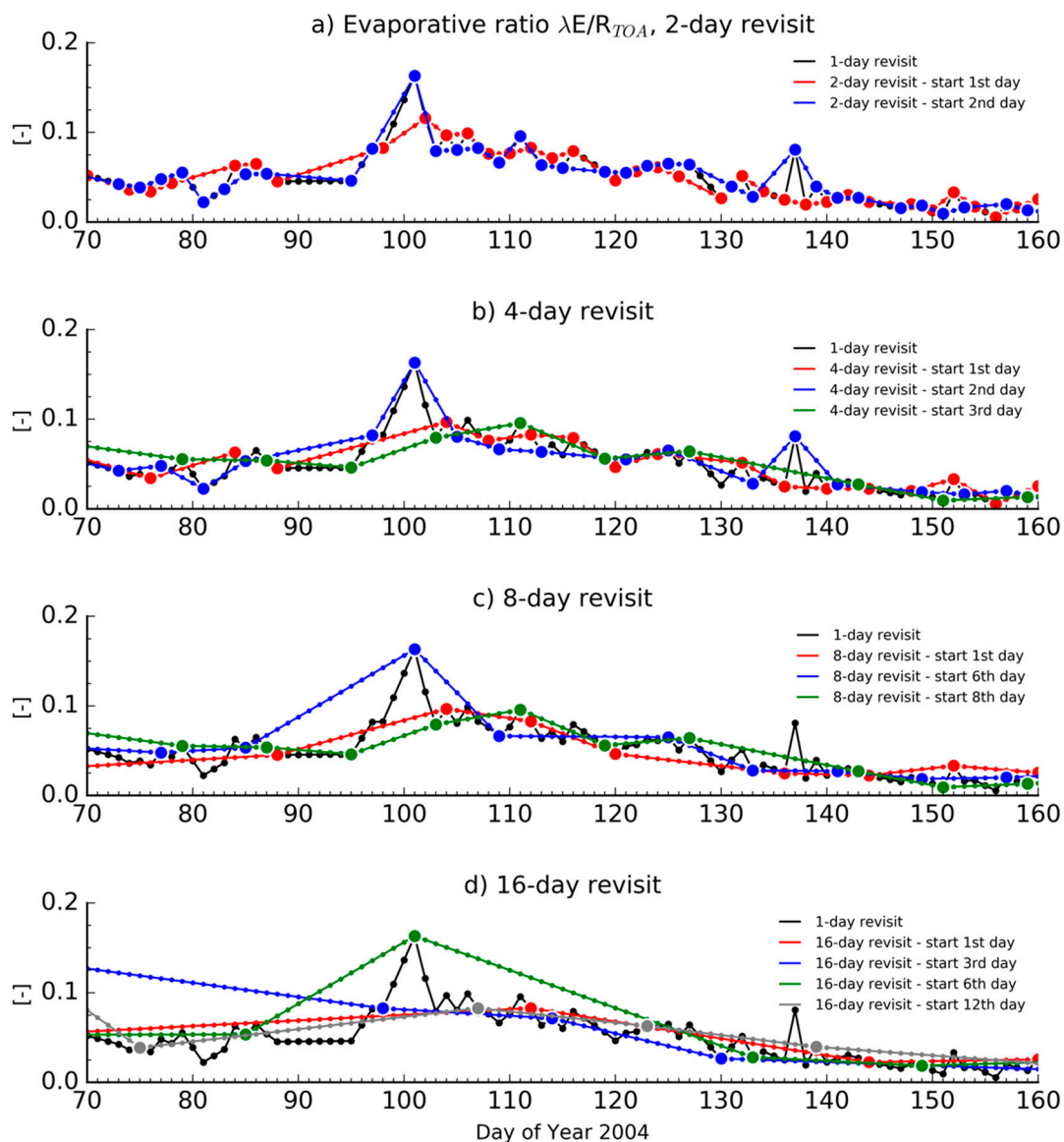


Figure 10. Cont.



**Figure 10.** Maximum discrepancies (in mm per day)—expressed as the median error (ME) plus three median absolute deviations (MAD)—between the one-day revisit monthly ET dataset and four different revisit scenarios (2-day, 4-day, 8-day and 16-day revisit) for each site and a 13:00 simulated satellite overpass time. The blue line represents the ET monthly average (in mm per day) derived from the one-day revisit dataset.

The effect of a single precipitation event on evaporative ratios estimates is illustrated at Audubon Ranch with data collected in spring 2004 (Figure 11). At Audubon, the rainfalls are not frequent in April, and the cumulated precipitation for April is usually low and less than 10 mm during normal years. In April 2004, the station measured a strong precipitation event of 50 mm of rainwater for a few days. This event was followed by a two-day period with large ET, up to 3.2 mm per day, mainly due to the high contribution of soil evaporation on total ET after a rain, and a longer period (around 30 days) with plant transpiration. In this case, the maximum deviations from the reference datasets corresponded to realizations of the 8-day and 16-day revisit scenarios that were able to capture the peak of evapotranspiration after the event (Figure 11).



**Figure 11.** Evaporative ratio calculated for different revisit scenarios (a to d: 2, 4, 8 or 16-day) using 13:00 data collected at Audubon Ranch, AZ from DOY 70 (10 March) to 160 (8 June) of 2004. For a given realization of a n-day revisit period scenario ( $n = 1, 2, 4, 8$  or  $16$ ), the larger markers represent clear sky observations, and the smaller markers represent days with no satellite observations (due to return period or clouds) associated with evaporative ratios estimated from two consecutive clear sky observations using linear interpolation. For a given n-day revisit scenario, the different realizations show the impact of precipitation events that occurred in April 2004.

Indeed, this local maximum was not representative of the April surface hydrology and revisit scenarios of eight days and up which strongly relied on temporal interpolation tended to then overestimate monthly ET. Depending on the day of initialization, maximum differences in monthly average ET in April 2004 were 0.03, 0.08 mm, 0.35 mm, and 0.7 mm per day for a 2, 4, 8 and 16-day revisit scenarios, respectively, representing around 2%, 7%, 31% and 61% of the monthly mean derived from the one-day dataset (i.e., 1.14 mm per day), respectively. The largest discrepancies were due to coarse samplings of the evaporative ratio (Figure 11) and interpolation procedures to estimate missing data that were not able to well represent individual and rapid events. For actual applications, such unrealistic cases should be identified and flagged by using additional information, such as the

rainfall climatology or cloud cover dynamic. When ET did not vary significantly with time, e.g., low ET values in May 2004, the different sampling scenarios provided very similar results.

## 4. Discussion

### 4.1. Scaling ET from Instantaneous Observations to Daytime Averages

The analysis of different scaling methods showed that the daytime self-preservation of evaporative ratios based on the available energy (AE), surface solar radiation ( $R_G$ ), top-of-atmosphere irradiance ( $R_{TOA}$ ) or potential evapotranspiration reference (PET) fluxes was usually not verified throughout the year for all the sites as already noted by other authors, such as References [4,36,43], for example. Similar to previous studies based on noon observations [33,34,40], we observed on average an underestimation of daytime ET derived from scaling methods using observations at 10:00 and 13:00.

Anderson et al. [4] used a constant  $\beta$  factor of 1.1 to compensate for underestimation of daytime total ET estimated using the evaporative fraction (i.e.,  $\beta_{AE}$ ) measured at midday. Following these results, Cammalleri et al. [38] applied the same correction to the evaporative fraction in an inter-comparison study of scaling methods. On average over all the sites, we found that the  $\beta$  factor varied from 0.93 to 1.18 (0.99 to 1.19, respectively) when derived from observations at 10:00 (13:00, respectively), depending on the scaling reference flux used. In comparison to the value used by Anderson et al. [4], we found an average  $\beta_{AE}$  factor of 1.18 and 1.17 when based on 10:00 and 13:00 measurements. In our study, the scaling method based on top-of-atmosphere irradiance ( $R_{TOA}$ ) was associated with  $\beta$  factor closer to one and similar or lower median errors than the other methods (Table 3). It should be noted that observed median errors and median absolute deviations were relatively low for all the methods, especially when considering the methods based on radiation fluxes ( $R_G$  and  $R_{TOA}$ ). Similar results had been found by Delogu et al. [35] and Ryu et al. [39]. Such results partly explained why no unique method has been clearly identified and selected yet by the scientific community for daytime scaling. Existing studies have already illustrated good performances of each of the four methods selected in this paper (see Table 1). For example, Cammalleri et al. [38] found that the incoming surface shortwave radiation  $R_G$  was the most robust scaling flux and found higher bias when using PET, while Tang et al. [37] found the best performance when using a scaling method based on PET.

The effect of the acquisition time on the median error and deviation associated with the different scaling methods depended on the experimental sites (Table A1 in Appendix A). On average, we found smaller median errors and median absolute deviations in daytime average ET when the scaling methods are based on data collected at 13:00 (Table 3).  $\beta$  factors were also closer to unity. Results are in line with Lagouarde et al. [16] who also showed that time-of-day to daytime ET scaling methods provided the best performance for satellite overpass around 13:00.

To derive surface ET at a larger scale using remote sensing data, it is necessary to estimate time-of-day ET at the satellite overpass time concurrently with time-of-day and daytime total values of the scaling reference flux. The evaporative fraction (i.e., AE is the scaling flux) has already been used by multiple ET retrieval algorithms based on remote sensing data, for example [4,9,10,15,83,84]. As already mentioned by Zhang and Lemeur [34], Van Niel et al. [36] and Ryu et al. [39], the evaporative ratio based on  $R_{TOA}$  can be accurately derived from a simple formula and represents a viable alternative for large-scale hydrological applications. Of all the methods we tested, our results verified those from Ryu et al. [39] and suggested that the scaling based on modeled  $R_{TOA}$  might be a very good candidate for large-scale remote sensing applications. Moreover, the method based on modeled  $R_{TOA}$  slightly outperformed the other methods.

### 4.2. Impact of the Satellite Revisit Period on ET Estimates

We showed that the impact of the revisit on ET depended on multiple factors, such as the local seasonal climate and land cover type. Therefore, the revisit period—a critical specification for missions



that propose to retrieve ET from remote sensing data—strongly depends on the objective of the missions. Globally, the average impact of the revisit on seasonal ET (as represented by the mean RMSE calculated over a multi-year dataset) depended on the season and varied from 16%, 13%, and 18% for a two-day revisit to 41%, 31% and 43% for a 16-day revisit in spring, summer and fall, respectively, based on observations at 13:00 (Figure 6). Results were derived from clear-sky ground measurements collected by 21 AmeriFlux towers distributed in the USA and they represented average conditions observed at those sites. Previous studies performed for Europe revealed a much smaller availability of cloud-free observations over northern regions [55], for example. On average, we found that four-day revisit systems should provide a significant improvement in temporal sampling to monitor surface ET reducing by around 40% the uncertainty of ET products derived from a 16-day system, such as Landsat (Table A2 in Appendix A). Driven by agricultural and water resources management applications, the nominal uncertainty requirements for satellite-based ET products specified by the Meteosat Second Generation Program [82] is 25% when evapotranspiration is higher than 0.4 mm per hour, and equal to 0.1 mm per hour otherwise, with a minimum requirement of 30%. Based on our results, a 30% uncertainty requirement on multi-year seasonal ET average was almost verified by a 16-day revisit period in summer (i.e., 31% based on 13:00 observations) and was only verified by a four-day revisit in spring and fall when accounting for the full dataset.

Relatively high RMSE values were observed between the one-day and two-day revisit scenarios (around 16% depending on the season—see Figure 6) clearly illustrates the fact that missing observations due to cloud coverage or orbital characteristics strongly impact the quality of the retrievals as already mentioned by Lagouarde et al. [16]. Based on statistical cloudiness analysis over Western Europe during spring and summer periods, Lagouarde et al. [16,55] showed that the average period of time without any cloud-free data varied from 5 to 10 days for a one-day revisit period, and up to 20 days for a two-day revisit. For these regions, the authors concluded that only a one-day revisit system was able to assess at field scale the rapid changes in surface hydrology after a specific rainfall or irrigation event. For precipitation events associated with short drying periods, we also found that rapid changes in surface hydrology could be partially captured by a two-day revisit instrument or totally missed by a four-day system. At Audubon Ranch, AZ in April 2004 for example, one of the two realizations of the two-day revisit scenario was not able to fully capture the short drying period after the event (red line in Figure 11a). However, in such a case and for revisit periods lower than four days, the short drying period did not significantly affect the monthly or seasonal mean, and the relevance of an impact of the revisit period might depend on the desired application. Most realizations of the 8-day and 16-day revisit scenarios were missing the drying period, but provided monthly total average close to the reference dataset. Therefore, return periods of eight days or more are not fully appropriate to daily operational management, such as irrigation scheduling. On the other hand, the realizations of the 8- and 16-day revisit scenarios that were able to capture the drying period were associated with strong discrepancies with the reference due to interpolation process of missing data due to the revisit and cloudiness. For most of the sites, we found that the maximum observed deviation of ET from the one-day revisit dataset—described by the median error plus three median absolute deviation of monthly average in our experiment—was lower than 1 mm per day for revisit periods of two days only (Figure 10). For agricultural sites, a four-day return period was associated with the maximum deviation of monthly ET average varying from 1 to 1.75 mm per day during the crop season (Figure 10). At most of the sites, the percentage of cloudy observations was slightly higher in the afternoon, but we did not find significant and systematic differences between the impact of the revisit on daytime ET based on observations made at 10:00 and 13:00. In comparison with the study by Delogu et al. [35], we found a larger sensitivity of the uncertainty on daytime ET estimates to changes in the revisit period. Using two two-year ground-based datasets collected in France and a one-year dataset collected in Morocco, Delogu et al. [35] found that revisit periods lower than six days had no significant impact on the estimation of seasonal average ET based on the evaporative fraction scaling method, probably reflecting a low temporal variability of surface hydrology. Nevertheless, while we found that the revisit



was critical to capture rapid changes in surface hydrology, the revisit was a less essential parameter to derive ET at yearly or seasonal time scales. Therefore, the relevance of sensitivity studies and ET uncertainty assessment strongly depends on the application.

This study was based on in situ observations, which implied the assumption of a perfect ET retrieval algorithm (i.e., latent heat fluxes are derived from in-situ observations associated with lower uncertainty than remote sensing retrievals) using perfect land surface temperature (LST) measurements from space, whereas LST retrievals can be prone to large uncertainties (several K) due to atmospheric corrections, emissivity and directional effects for instance [85,86]. Consequently, expected uncertainties associated with actual satellite-based ET products may be higher than those reported in this paper. For example, reviews of satellite-based ET validation studies [14,87,88] reported average uncertainty on derived ET of around 0.8 mm per day. Based on a review of 33 research articles, Karimi and Bastiaanssen [89] reported that the error associated with remote sensing-based ET estimates varied from 1% to 20% depending on the land surface type and local climate with a mean relative error of around 5% and a standard deviation of 5%.

For a given revisit, the uncertainty on ET estimates (i.e., RMSE) may depend on the interpolation procedure used to fill the gaps between two consecutive clear-sky observations. We chose a linear interpolation technique (of the evaporative fraction) for its simplicity. Intermediate results (not described in this paper) suggested that spline or bilinear interpolation methods were less appropriate to represent rapid changes in surface hydrology measured by the stations. Therefore, temporal interpolation and disaggregation strategies based on blended remote sensing products derived from systems at different temporal resolutions, e.g., the Disaggregation of the Radiometric Temperature (DisTrad) method [90,91], the Disaggregation of Evaporative Fraction (DEFrac) [91,92] and the Spatial and Temporal Adaptive Reflectance Fusion Model (STARFM) [93,94], have been successfully used to improve ET estimates at high spatial resolution for precision agriculture applications. Bindhu et al. [95] were able to disaggregate MODIS LST products at 1 km to the resolution of Landsat 7 (60 m) with an RMSE lower than 0.96 K using a refined version of DisTrad (NL-DisTrad). To some extent, such techniques help to reduce uncertainties due to temporal interpolation. However, datasets with a higher temporal resolution usually have a coarser spatial resolution that can introduce uncertainties due to spatial variability of LST within pixels at km scale [96,97].

## 5. Conclusions

We used Ameriflux data to evaluate the performance of four different methods commonly used to scale ET from time-of-day observations to daytime averages and quantify the impact of the revisit period of observational systems on ET uncertainty. We found that the different methods performed relatively well and the observed differences with ground-based measurements were associated with low median errors and median absolute deviations. The scaling method based on the top-of-atmosphere solar radiation ( $R_{TOA}$ ) ensured slightly better performance than the other methods (i.e.,  $\beta$  factor closer to unity and lower median errors on average). Moreover, the scaling method based on modeled  $R_{TOA}$  does not require ancillary information (only time, date and location) and might be very suitable for large-scale remote sensing applications. Uncertainties of daytime ET estimates increased with longer revisit times and the impact of different revisit periods depended on the land cover type and local climate. During spring, summer and fall, a five-day revisit scenario was associated with 30% or less uncertainty on seasonal ET average. For most of our sites, we did not find significant and systematic differences between the impact of the revisit on daytime ET based on observations made at 10:00 and 13:00. On average, we found that four- or five-day revisit systems may provide a significant improvement in temporal sampling to monitor surface ET reducing by around 40% the uncertainty of ET products derived from a 16-day revisit system, such as Landsat. The capability to capture the contribution of rapid changes in moisture events to surface hydrology and ET was significantly reduced for return periods of eight days or more. As already mentioned by Anderson et al. [12], a four-day revisit system could be achieved by using a constellation of four different Landsat satellites.

With return periods of five days or less, NASA ECOSTRESS represents a significant improvement in terms of temporal sampling of land surface temperature required to derive reliable ET products at the field scale. Onboard the International Space Station, ECOSTRESS is monitoring the Earth's surface with various overpass and revisit times, depending on the latitude allowing scaling methods and the impact of overpass time on ET retrievals to be further examined.

**Author Contributions:** Conceptualization, P.C.G. and S.J.H.; methodology, P.C.G. and A.O.; software, P.C.G.; formal analysis, all authors; writing—original draft preparation, P.C.G.; writing—review and editing, all authors; funding acquisition, P.C.G., S.J.H., J.-P.L. and E.F.V.

**Funding:** The research described in this paper was carried out at the Jet Propulsion Laboratory, California Institute of Technology, Pasadena, CA, and at the University of Maryland under contracts with the National Aeronautics and Space Administration (NASA). The study was supported by the ROSES 2016 Applied Research—Water Resources Program (NRA NNH16ZDA001N), the NASA Terrestrial Hydrology Program, and the HypIRI and ECOSTRESS projects. This work was supported in France by the Centre National d'Études Spatiales (CNES, the French Space Agency) through the TOSCA (Terre, Océan, Surfaces Continentales, Atmosphère) committee in the frame of the THIRSTY preparation program and by the Programme National de Télédétection Spatiale (n° PNTS-2015-11).

**Acknowledgments:** The authors kindly thank Michael B. Mercury for providing the statistics for cloud coverage from MODIS observations. The authors thank the principal investigators of the AmeriFlux sites: Dennis Baldocchi, Nathaniel Brunsell, Lianhong Gu, Jim Heilman, Roser Matamala, Tilden Meyers, Asko Noormets, Clenton Owensby, Steve Pallardy, Russell Scott, Andy Suyker, and Margaret Torn. In addition, funding for AmeriFlux data resources was provided by the U.S. Department of Energy's Office of Science. AmeriFlux data are available online at <http://ameriflux.ornl.gov/> from Oak Ridge National Laboratory (ORNL) Distributed Active Archive Center (DAAC), Oak Ridge, Tennessee, U.S.A.

**Conflicts of Interest:** The authors declare no conflict of interest. The funders had no role in the design of the study; in the collection, analyses, or interpretation of data; in the writing of the manuscript, or in the decision to publish the results.

## Appendix A

**Table A1.**  $\beta$  factors derived from observations made at 10:00 and 13:00 for each site and different reference scaling fluxes: the available energy (AE), surface solar radiation ( $R_G$ ), simulated top-of-atmosphere solar radiation ( $R_{TOA}$ ) and potential evapotranspiration (PET). The AmeriFlux site ID labels are defined in Table 2. Two agricultural sites near Mead, NE (i.e., Ne1 and Ne2) represent irrigated crops.

Site ID	10:00 Overpass				13:00 Overpass			
	AE	$R_G$	$R_{TOA}$	PET	AE	$R_G$	$R_{TOA}$	PET
ARM	1.24	1.11	0.98	1.10	1.15	1.01	0.93	1.14
Aud	1.40	1.09	0.89	1.18	1.32	1.12	1.07	1.29
Bo1	1.25	1.11	0.87	1.15	1.07	1.00	0.96	1.11
Bkg	1.28	1.14	0.98	1.15	1.14	1.02	0.94	1.17
ChR	1.22	1.13	1.00	1.12	1.12	1.03	0.91	1.14
IB1	1.04	1.13	0.86	1.14	1.08	1.02	1.00	1.14
IB2	1.14	1.09	0.84	1.11	1.08	1.02	0.98	1.13
Fpe	1.42	1.13	0.88	1.24	1.15	1.05	0.96	1.20
FR2	1.10	1.10	0.94	1.09	1.20	1.12	1.01	1.17
FR3	1.03	0.99	0.97	0.95	1.27	1.19	1.08	1.26
Kon	1.15	1.06	1.00	1.01	1.27	1.11	1.02	1.22
NC2	1.20	1.11	0.90	1.14	1.13	1.02	0.96	1.14
NC1	1.23	1.11	0.89	1.14	1.15	1.04	0.97	1.17
Ne1	1.13	1.09	0.92	1.10	1.13	1.04	0.98	1.17
Ne2	1.11	1.07	0.90	1.08	1.16	1.07	1.00	1.20

Table A1. Cont.

Site ID	10:00 Overpass				13:00 Overpass			
	AE	R <sub>G</sub>	R <sub>TOA</sub>	PET	AE	R <sub>G</sub>	R <sub>TOA</sub>	PET
Ne3	1.10	1.05	0.88	1.06	1.20	1.09	1.03	1.23
MOz	1.20	1.09	0.87	1.11	1.18	1.08	1.00	1.19
SRM	0.98	1.03	0.98	1.05	1.25	1.18	1.06	1.29
Ton	1.22	1.06	0.99	1.10	1.22	1.11	1.03	1.24
Var	1.30	1.12	1.03	1.17	1.25	1.08	1.00	1.25
WBW	1.24	1.17	1.04	1.18	1.10	1.03	0.91	1.12

**Table A2.** Mean ET RMSE in mm per day between a 2, 4, 8 or 16-day revisit scenario and the one-day revisit dataset based on ET observations made at 10:00 and 13:00 for different land cover types. Values in parentheses represent the relative errors (i.e., ratio between RMSE and seasonal average ET based on the one-day revisit dataset).

	Season	10:00				13:00			
		DJF	MAM	JJA	SON	DJF	MAM	JJA	SON
2-day revisit	All sites	0.132 (29%)	0.270 (18%)	0.373 (13%)	0.196 (18%)	0.103 (24%)	0.250 (16%)	0.371 (13%)	0.189 (18%)
	Cropland	0.101 (25%)	0.307 (21%)	0.439 (12%)	0.182 (16%)	0.090 (24%)	0.263 (19%)	0.378 (11%)	0.176 (17%)
	Grassland	0.109 (25%)	0.240 (16%)	0.364 (16%)	0.151 (18%)	0.091 (26%)	0.270 (17%)	0.359 (16%)	0.130 (17%)
	Broadleaf Forest	0.142 (42%)	0.256 (17%)	0.373 (12%)	0.219 (18%)	0.100 (31%)	0.226 (15%)	0.445 (13%)	0.253 (20%)
	Needleleaf Forest	0.187 (24%)	0.314 (13%)	0.406 (9%)	0.351 (16%)	0.156 (21%)	0.280 (12%)	0.522 (13%)	0.326 (16%)
	Woody Savannah	0.182 (29%)	0.228 (16%)	0.178 (11%)	0.184 (20%)	0.121 (20%)	0.189 (12%)	0.170 (11%)	0.147 (17%)
4-day revisit	All sites	0.181 (39%)	0.409 (27%)	0.550 (19%)	0.273 (25%)	0.146 (35%)	0.349 (23%)	0.549 (19%)	0.268 (26%)
	Cropland	0.149 (38%)	0.447 (30%)	0.626 (18%)	0.252 (22%)	0.146 (39%)	0.379 (27%)	0.571 (16%)	0.250 (24%)
	Grassland	0.162 (38%)	0.362 (25%)	0.524 (23%)	0.220 (26%)	0.117 (33%)	0.340 (22%)	0.510 (23%)	0.206 (27%)
	Broadleaf Forest	0.178 (53%)	0.402 (27%)	0.591 (19%)	0.344 (28%)	0.131 (41%)	0.338 (22%)	0.695 (21%)	0.373 (30%)
	Needleleaf Forest	0.268 (34%)	0.461 (20%)	0.592 (14%)	0.441 (21%)	0.213 (29%)	0.352 (15%)	0.673 (17%)	0.371 (18%)
	Woody Savannah	0.227 (36%)	0.383 (26%)	0.314 (19%)	0.226 (24%)	0.167 (28%)	0.302 (20%)	0.278 (19%)	0.215 (25%)
8-day revisit	All sites	0.228 (50%)	0.549 (36%)	0.728 (26%)	0.362 (33%)	0.189 (45%)	0.492 (33%)	0.735 (26%)	0.347 (33%)
	Cropland	0.189 (48%)	0.560 (38%)	0.822 (23%)	0.355 (31%)	0.186 (50%)	0.507 (36%)	0.774 (22%)	0.341 (32%)
	Grassland	0.194 (45%)	0.495 (34%)	0.684 (31%)	0.285 (34%)	0.155 (43%)	0.478 (31%)	0.670 (30%)	0.283 (37%)
	Broadleaf Forest	0.234 (69%)	0.636 (42%)	0.799 (26%)	0.423 (35%)	0.169 (53%)	0.558 (37%)	0.906 (27%)	0.438 (35%)
	Needleleaf Forest	0.331 (42%)	0.613 (26%)	0.806 (19%)	0.575 (27%)	0.273 (37%)	0.523 (23%)	0.929 (23%)	0.508 (25%)
	Woody Savannah	0.290 (46%)	0.489 (34%)	0.418 (25%)	0.318 (34%)	0.224 (38%)	0.389 (25%)	0.414 (28%)	0.268 (32%)

Table A2. Cont.

	Season	10:00				13:00			
		DJF	MAM	JJA	SON	DJF	MAM	JJA	SON
16-day revisit	All sites	0.285 (62%)	0.689 (45%)	0.924 (32%)	0.471 (43%)	0.237 (56%)	0.627 (41%)	0.901 (31%)	0.447 (43%)
	Cropland	0.261 (66%)	0.719 (49%)	1.017 (29%)	0.498 (43%)	0.230 (62%)	0.659 (47%)	0.967 (27%)	0.472 (45%)
	Grassland	0.239 (56%)	0.642 (44%)	0.880 (39%)	0.376 (44%)	0.202 (56%)	0.613 (39%)	0.833 (38%)	0.341 (45%)
	Broadleaf Forest	0.285 (84%)	0.805 (53%)	1.050 (34%)	0.527 (43%)	0.214 (68%)	0.690 (45%)	1.065 (32%)	0.552 (44%)
	Needleleaf Forest	0.408 (52%)	0.694 (29%)	1.007 (23%)	0.713 (33%)	0.331 (45%)	0.645 (28%)	1.083 (27%)	0.619 (30%)
	Woody Savannah	0.341 (54%)	0.567 (39%)	0.554 (34%)	0.370 (40%)	0.279 (47%)	0.493 (32%)	0.542 (36%)	0.340 (40%)

## References

- Chahine, M.T. The hydrological cycle and its influence on climate. *Nature* **1992**, *359*, 373–380. [\[CrossRef\]](#)
- Fisher, J.B.; Whittaker, R.; Malhi, Y. ET Come Home: Potential evapotranspiration in geographical ecology. *Glob. Ecol. Biogeogr.* **2011**, *20*, 1–18. [\[CrossRef\]](#)
- Fisher, J.B. Land-atmosphere interactions: Evapotranspiration. In *Encyclopedia of Remote Sensing*; Njoku, E., Ed.; Springer: Berlin/Heidelberg, Germany, 2013; pp. 1–5.
- Anderson, M.C.; Norman, J.M.; Diak, G.R.; Kustas, W.P.; Mecikalski, J.R. A two-source time-integrated model for estimating surface fluxes using thermal infrared remote sensing. *Remote Sens. Environ.* **1997**, *60*, 195–216. [\[CrossRef\]](#)
- Olioso, A.; Chauki, H.; Courault, D.; Wigneron, J.-P. Estimation of evapotranspiration and photosynthesis by assimilation of remote sensing data into SVAT models. *Remote Sens. Environ.* **1999**, *68*, 341–356. [\[CrossRef\]](#)
- Merchant, C.J.; Matthiessen, S.; Rayner, N.A.; Remedios, J.J.; Jones, P.D.; Olesen, F.; Trewin, B.; Thorne, P.W.; Auchmann, R.; Corlett, G.K.; et al. The Surface Temperatures of the Earth: Steps towards Integrated Understanding of Variability and Change. *Geosci. Instrum. Methods* **2013**, *2*, 305–321. [\[CrossRef\]](#)
- Fisher, J.B.; Melton, F.; Middleton, E.; Hain, C.; Anderson, M.; Allen, R.; McCabe, M.F.; Hook, S.; Baldocchi, D.; Townsend, P.A.; et al. The Future of Evapotranspiration: Global requirements for ecosystem functioning, carbon and climate feedbacks, agricultural management, and water resources. *Water Resour. Res.* **2017**, *53*, 2618–2626. [\[CrossRef\]](#)
- Anderson, M.C.; Hain, C.; Wardlow, B.; Pimstein, A.; Mecikalski, J.R.; Kustas, W.P. Evaluation of Drought Indices Based on Thermal Remote Sensing of Evapotranspiration over the Continental United States. *J. Clim.* **2011**, *24*, 2025–2044. [\[CrossRef\]](#)
- Fisher, J.B.; Tu, K.P.; Baldocchi, D.D. Global estimates of the land-atmosphere water flux based on monthly AVHRR and ISLSCP-II data, validated at 16 FLUXNET sites. *Remote Sens. Environ.* **2008**, *112*, 901–919. [\[CrossRef\]](#)
- Gallego-Elvira, B.; Olioso, A.; Mira, M.; Reyes-Castillo, S.; Boulet, G.; Marloie, O.; Garrigues, S.; Courault, D.; Weiss, M.; Chauvelon, P.; et al. EVASPA (EVApotranspiration Assessment from SPace) tool: An overview. *Procedia Environ. Sci.* **2013**, *19*, 303–310. [\[CrossRef\]](#)
- Mu, Q.; Zhao, M.; Kimball, J.S.; McDowell, N.G.; Running, S.W. A Remotely Sensed Global Terrestrial Drought Severity Index. *Bull. Am. Meteorol. Soc.* **2013**, *94*, 83–98. [\[CrossRef\]](#)
- Anderson, M.C.; Allen, R.G.; Morse, A.; Kustas, W.P. Use of Landsat thermal imagery in monitoring evapotranspiration and managing water resources. *Remote Sens. Environ.* **2012**, *122*, 50–65. [\[CrossRef\]](#)
- Allen, R.G.; Tasumi, M.; Trezza, R. Satellite-based energy balance for mapping evapotranspiration with internalized calibration (METRIC)-model. *J. Irrig. Drain. Eng.* **2007**, *133*, 380–394. [\[CrossRef\]](#)
- Bastiaanssen, W.G.M.; Noordman, E.J.M.; Pelgrum, H.; Davids, G.; Thoreson, B.P.; Allen, R.G. SEBAL Model with remotely sensed data to improve water resources management under actual field conditions. *J. Irrig. Drain. Eng.* **2005**, *131*, 85–93. [\[CrossRef\]](#)

15. Gómez, M.; Olioso, A.; Sobrino, J.A.; Jacob, F. Retrieval of evapotranspiration over the Alpillés/ReSeDA experimental site using airborne POLDER sensor and a thermal camera. *Remote Sens. Environ.* **2005**, *96*, 399–408. [\[CrossRef\]](#)
16. Lagouarde, J.-P.; Bach, M.; Sobrino, J.A.; Boulet, G.; Briottet, X.; Cherchali, S.; Coudert, B.; Dadou, I.; Dedieu, G.; Gamet, P.; et al. The MISTIGRI thermal infrared project: Scientific objectives and mission specifications. *Int. J. Remote Sens.* **2013**, *34*, 3437–3466. [\[CrossRef\]](#)
17. Allen, R.G.; Pereira, L.S.; Howell, T.A.; Jensen, M.E. Evapotranspiration information reporting: I. Factors governing measurement accuracy. *Agric. Water Manag.* **2011**, *98*, 899–920. [\[CrossRef\]](#)
18. Fisher, J.B.; Hook, S.; Allen, R.; Anderson, M.; French, A.; Hain, C.; Hulley, G.; Wood, E. The ECOSystem Spaceborne Thermal Radiometer Experiment on Space Station (ECOSTRESS): Science motivation. In Proceedings of the American Geophysical Union (AGU) Fall Meeting, San Francisco, CA, USA, 15–19 December 2014.
19. Fisher, J.B.; Hook, S.; Allen, R.; Anderson, M.; French, A.; Hain, C.; Hulley, G.; Wood, E. ECOSTRESS: NASA's next-generation mission to measure evapotranspiration from the International Space Station. In Proceedings of the American Geophysical Union (AGU) Fall Meeting, San Francisco, CA, USA, 14–18 December 2015.
20. ECOSTRESS. Available online: <http://ecostress.jpl.nasa.gov> (accessed on 29 December 2018).
21. Lee, C.M.; Cable, M.L.; Hook, S.J.; Green, R.O.; Ustin, S.L.; Mandl, D.J.; Middleton, E.M. An introduction to the NASA Hyperspectral Infrared Imager (HypIRI) mission and preparatory activities. *Remote Sens. Environ.* **2015**, *167*, 6–19. [\[CrossRef\]](#)
22. Koetz, B.; Bastiaanssen, W.; Berger, M.; Defournay, P.; Del Bello, U.; Drusch, M.; Drinkwater, M.; Duca, R.; Fernandez, V.; Ghent, D.; et al. High Spatio-Temporal Resolution Land Surface Temperature Mission—A Copernicus candidate mission in support of agricultural monitoring. In Proceedings of the IEEE International Geoscience and Remote Sensing Symposium (IGARSS), Valencia, Spain, 22–27 July 2018. [\[CrossRef\]](#)
23. Lagouarde, J.-P.; Bhattacharya, B.K.; Crébassol, P.; Gamet, P.; Babu, S.S.; Boulet, G.; Briottet, X.; Buddhiraju, K.M.; Cherchali, S.; Dadou, I.; et al. The Indian-French Trishna Mission: Earth Observation in the Thermal Infrared with High Spatio-Temporal Resolution. In Proceedings of the IEEE International Geoscience and Remote Sensing Symposium (IGARSS), Valencia, Spain, 22–27 July 2018. [\[CrossRef\]](#)
24. Mercury, M.; Green, R.; Hook, S.; Oaida, B.; Wu, W.; Gunderson, A.; Chodas, M. Global cloud cover for assessment of optical satellite observation opportunities: A HypIRI case study. *Remote Sens. Environ.* **2012**, *126*, 62–71. [\[CrossRef\]](#)
25. Lagouarde, J.-P.; Irvine, M.; Dupont, S. Atmospheric turbulence induced errors on measurements of surface temperature from space. *Remote Sens. Environ.* **2015**, *68*, 40–53. [\[CrossRef\]](#)
26. Alfieri, J.G.; Anderson, M.C.; Kustas, W.P.; Cammalleri, C. Effect of the revisit interval and temporal upscaling methods on the accuracy of remotely sensed evapotranspiration estimates. *Hydrol. Earth Syst. Sci.* **2017**, *21*, 83–98. [\[CrossRef\]](#)
27. Kustas, W.P.; Perry, E.M.; Doraiswamy, P.C.; Moran, M.S. Using satellite remote sensing to extrapolate evapotranspiration estimates in time and space over a semiarid rangeland basin. *Remote Sens. Environ.* **1994**, *49*, 275–286. [\[CrossRef\]](#)
28. Bastiaanssen, W.G.M.; Molden, D.J.; Makin, I.W. Remote sensing for irrigated agriculture: Examples from research and possible applications. *Agric. Water Manag.* **2000**, *46*, 137–155. [\[CrossRef\]](#)
29. Anderson, M.C.; Kustas, W.P.; Norman, J.M.; Hain, C.R.; Mecikalski, J.R.; Schultz, L.; Gonzalez-Dugo, M.P.; Cammalleri, C.; d'Urso, G.; Pimstein, A.; et al. Mapping daily evapotranspiration at field to continental scales using geostationary and polar orbiting satellite imagery. *Hydrol. Earth Syst. Sci.* **2011**, *15*, 223–239. [\[CrossRef\]](#)
30. Shuttleworth, W.J.; Gurney, R.J.; Hsu, A.Y.; Ormsby, J.P. FIFE, the variation on energy partition at surface flux sites. In Proceedings of the International Association of Hydrological Sciences (IAHS) Third Scientific Assembly, Baltimore, MD, USA, 10–19 May 1989; pp. 67–74.
31. Shuttleworth, W.J. The Modelling concept. *Rev. Geophys.* **1991**, *29*, 585–606. [\[CrossRef\]](#)
32. Jackson, R.D.; Hatfield, J.L.; Reginato, R.J.; Idso, S.B.; Pinter, P.J. Estimation of daily evapotranspiration from one time of day measurements. *Agric. Water Manag.* **1983**, *7*, 351–362. [\[CrossRef\]](#)
33. Brutsaert, W.; Sugita, M. Application of self-preservation in the diurnal evolution of the surface energy budget to determine daily evaporation. *J. Geophys. Res.* **1992**, *97*, 18377–18382. [\[CrossRef\]](#)



34. Zhang, L.; Lemeur, R. Evaluation of daily evaporation estimates from instantaneous measurements. *Agric. For. Meteorol.* **1995**, *74*, 139–154. [\[CrossRef\]](#)
35. Delogu, E.; Boulet, G.; Olioso, A.; Coudert, B.; Chirouze, J.; Ceschia, E.; Le Dantec, V.; Marloie, O.; Chehbouni, G.; Lagouarde, J.-P. Reconstruction of temporal variations of evapotranspiration using instantaneous estimates at the time of satellite overpass. *Hydrol. Earth Syst. Sci.* **2012**, *16*, 2995–3010. [\[CrossRef\]](#)
36. Van Niel, T.G.; McVicar, T.R.; Roderick, M.L.; van Dijk, A.I.J.M.; Beringer, J.; Hutley, L.B.; van Gorsel, E. Upscaling latent heat flux for thermal remote sensing studies: Comparison of alternative approaches and correction of bias. *J. Hydrol.* **2012**, *468–469*, 35–46. [\[CrossRef\]](#)
37. Tang, R.; Li, Z.-L.; Sun, X. Temporal upscaling of instantaneous evapotranspiration: An intercomparison of four methods using eddy covariance measurements and MODIS data. *Remote Sens. Environ.* **2013**, *138*, 102–118. [\[CrossRef\]](#)
38. Cammalleri, C.; Anderson, M.C.; Kustas, W.P. Upscaling of evapotranspiration fluxes from instantaneous to daytime scales for thermal remote sensing applications. *Hydrol. Earth Syst. Sci.* **2014**, *18*, 1885–1894. [\[CrossRef\]](#)
39. Ryu, Y.; Baldocchi, D.D.; Black, T.A.; Detto, M.; Law, B.E.; Leuning, R.; Miyata, A.; Reichstein, M.; Vargas, R.; Ammann, C.; et al. On the temporal upscaling of evapotranspiration from instantaneous remote sensing measurements to 8-day mean daily-sums. *Agric. For. Meteorol.* **2012**, *152*, 212–222. [\[CrossRef\]](#)
40. Crago, R.D. Conservation and variability of the evaporative fraction during the daytime. *J. Hydrol.* **1996**, *180*, 173–194. [\[CrossRef\]](#)
41. Sobrino, J.; Gomez, M.; Jimenez-Munoz, J.; Olioso, A. Application of a simple algorithm to estimate daily evapotranspiration from NOAA-AVHRR images for the Iberian Peninsula. *Remote Sens. Environ.* **2007**, *110*, 139–148. [\[CrossRef\]](#)
42. Hoedjes, J.C.B.; Chehbouni, A.; Jacob, F.; Ezzahar, J.; Boulet, G. Deriving daily evapotranspiration from remotely sensed instantaneous evaporative fraction over olive orchard in semi-arid Morocco. *J. Hydrol.* **2008**, *354*, 53–64. [\[CrossRef\]](#)
43. Crago, R.D.; Brutsaert, W. Daytime evaporation and the self-preservation of the evaporative fraction and the Bowen ratio. *J. Hydrol.* **1996**, *178*, 241–255. [\[CrossRef\]](#)
44. Gentine, P.; Entekhabi, D.; Chehbouni, A.; Boulet, G.; Duchemin, B. Analysis of evaporative fraction diurnal behaviour. *Agric. For. Meteorol.* **2007**, *143*, 13–29. [\[CrossRef\]](#)
45. Van Niel, T.G.; McVicar, T.R.; Roderick, M.L.; van Dijk, A.I.J.M.; Renzullo, L.J.; van Gorsel, E. Correcting for systematic error in satellite-derived latent heat flux due to assumptions in temporal scaling: Assessment from flux tower observations. *J. Hydrol.* **2011**, *409*, 140–148. [\[CrossRef\]](#)
46. Sugita, M.; Brutsaert, W. Daily evaporation over a region from lower boundary layer profiles measured with radiosondes. *Water Resour. Res.* **1991**, *27*, 747–752. [\[CrossRef\]](#)
47. Stannard, D.I.; Blanford, J.H.; Kustas, W.P.; Nichols, W.D.; Amer, S.A.; Schmugge, T.J.; Welt, M.A. Interpretation of surface-flux measurements in heterogeneous terrain during Monsoon '90 experiment. *Water Resour. Res.* **1994**, *30*, 1227–1239. [\[CrossRef\]](#)
48. Baldocchi, D.D.; Falge, E.; Gu, L.; Olson, R.; Hollinger, D.; Running, S.; Anthoni, P.; Bernhofer, C.; Davis, K.; Evans, R.; et al. Fluxnet: A new tool to study the temporal and spatial variability of ecosystem-scale carbon dioxide, water vapor, and energy flux densities. *Bull. Am. Meteorol. Soc.* **2001**, *82*, 2415–2434. [\[CrossRef\]](#)
49. Penman, H.L. Natural evaporation from open water, bare soil and grass. *Proc. R. Soc. Lond.* **1948**, *193*, 120–145.
50. Shuttleworth, W.J. Evaporation. In *Handbook of Hydrology*; Maidment, D.R., Ed.; McGraw-Hill: Sydney, Australia, 1993; Chapter 4.
51. McVicar, T.R.; Roderick, M.L.; Donohue, R.J.; Li, L.T.; Van Niel, T.G.; Thomas, A.; Grieser, J.; Jhajharia, D.; Himri, Y.; Mahowald, N.M.; et al. Global review and synthesis of trends in observed terrestrial near-surface wind speeds: Implications for evaporation. *J. Hydrol.* **2012**, *416–417*, 182–205. [\[CrossRef\]](#)
52. Donohue, R.J.; McVicar, T.R.; Roderick, M.L. Assessing the ability of potential evaporation formulations to capture the dynamics in evaporative demand within a changing climate. *J. Hydrol.* **2010**, *386*, 186–197. [\[CrossRef\]](#)
53. McVicar, T.R.; Roderick, M.L.; Donohue, R.J.; Van Niel, T.G. Less bluster ahead? Overlooked ecohydrological implications of global trends of terrestrial near-surface wind speeds. *Ecohydrology* **2012**, *5*, 381–388. [\[CrossRef\]](#)

54. Delogu, E.; Boulet, G.; Oliso, A.; Garrigues, S.; Brut, A.; Tallec, T.; Demarty, J.; Soudani, K.; Lagouarde, J.-P. Evaluation of the SPARSE dual-source model for predicting water stress and evapotranspiration from thermal infra-red data over multiple crops and climates. *Remote Sens.* **2018**, *10*, 1806. [\[CrossRef\]](#)
55. Lagouarde, J.-P.; Oliso, A.; Roujean, J.-L.; Boulet, G.; Coudert, B.; Dayau, S.; Castillo, S.; Weiss, M. Defining the revisit frequency for the MISTIGRI project of a satellite mission in the thermal infrared. In Proceedings of the 3rd International Symposium “Recent Advances in Quantitative Remote Sensing”, Valencia, Spain, 27 September–1 October 2010; pp. 824–829.
56. Leys, C.; Ley, C.; Klein, O.; Bernard, P.; Licata, L. Detecting outliers: Do not use standard deviation around the mean, use absolute deviation around the median. *J. Exp. Soc. Psychol.* **2013**, *49*, 764–766. [\[CrossRef\]](#)
57. Billesbach, D.P.; Fischer, M.L.; Torn, M.S.; Berry, J.A. A Portable Eddy Covariance System for the Measurement of Ecosystem-Atmosphere Exchange of CO<sub>2</sub>, Water Vapor, and Energy. *J. Atmos. Ocean. Technol.* **2004**, *21*, 639–650. [\[CrossRef\]](#)
58. Krishnan, P.; Meyers, T.P.; Scott, R.L.; Kennedy, L.; Heuer, M. Energy exchange and evapotranspiration over two temperate semi-arid grasslands in North America. *Agric. For. Meteorol.* **2012**, *153*, 31–44. [\[CrossRef\]](#)
59. Meyers, T.P.; Hollinger, S.E. An assessment of storage terms in the surface energy balance of maize and soybean. *Agric. For. Meteorol.* **2004**, *125*, 105–115. [\[CrossRef\]](#)
60. Hollinger, D.Y.; Ollinger, S.V.; Richardson, A.D.; Meyers, T.P.; Dail, D.B.; Martin, M.E.; Scott, N.A.; Arkebauer, D.; Baldocchi, D.; Clark, K.L.; et al. Albedo estimates for land surface models and support for a new paradigm based on foliage nitrogen concentration. *Glob. Chang. Biol.* **2010**, *16*, 696–710. [\[CrossRef\]](#)
61. Matamala, R.; Jastrow, J.D.; Miller, R.M.; Garten, C.T. Temporal changes in C and N stocks of restored prairie: Implications for C sequestration strategies. *Ecol. Appl.* **2008**, *18*, 1470–1488. [\[CrossRef\]](#) [\[PubMed\]](#)
62. Gilmanov, T.G.; Tieszen, L.L.; Wylie, B.K.; Flanagan, L.B.; Frank, A.B.; Haferkamp, M.R.; Meyers, T.P.; Morgan, J.A. Integration of CO<sub>2</sub> flux and remotely-sensed data for primary production and ecosystem respiration analyses in the Northern Great Plains: Potential for quantitative spatial extrapolation. *Glob. Ecol. Biogeogr.* **2005**, *14*, 271–292. [\[CrossRef\]](#)
63. Heinsch, F.A.; Heilman, J.L.; McInnes, K.J.; Cobos, D.R.; Zuberer, D.A.; Roelke, D.L. Carbon dioxide exchange in a high marsh on the Texas Gulf Coast: Effects of freshwater availability. *Agric. For. Meteorol.* **2004**, *125*, 159–172. [\[CrossRef\]](#)
64. Brunsell, N.A.; Ham, J.M.; Owensby, C.E. Assessing the multi-resolution information content of remotely sensed variables and elevation for evapotranspiration in a tall-grass prairie environment. *Remote Sens. Environ.* **2008**, *112*, 2977–2987. [\[CrossRef\]](#)
65. Noormets, A.; Gavazzi, M.J.; McNulty, S.G.; Domec, J.-C.; Sun, G.; King, J.S.; Chen, J. Response of carbon fluxes to drought in a coastal plain loblolly pine forest. *Glob. Chang. Biol.* **2010**, *16*, 272–287. [\[CrossRef\]](#)
66. Verma, S.B.; Dobermann, A.; Cassman, K.G.; Walters, D.T.; Knops, J.M.; Arkebauer, T.J.; Suyker, A.E.; Burba, G.G.; Amos, B.; Yang, H.S.; et al. Annual carbon dioxide exchange in irrigated and rainfed maize-based agroecosystems. *Agric. For. Meteorol.* **2005**, *131*, 77–96. [\[CrossRef\]](#)
67. Gu, L.H.; Meyers, T.; Pallardy, S.G.; Hanson, P.J.; Yang, B.; Heuer, M.; Hosman, K.P.; Liu, Q.; Riggs, J.S.; Sluss, D.; et al. Influences of biomass heat and biochemical energy storages on the land surface fluxes and radiative temperature. *J. Geophys. Res.* **2007**, *112*, D02107. [\[CrossRef\]](#)
68. Scott, R.L.; Jenerette, G.D.; Potts, D.L.; Huxman, T.E. Effects of seasonal drought on net carbon dioxide exchange from a woody-plantencroached semiarid grassland. *J. Geophys. Res. Biogeogr.* **2009**, *114*, G04004. [\[CrossRef\]](#)
69. Baldocchi, D.D.; Xu, L.K.; Kiang, N. How plant functional-type, weather, seasonal drought, and soil physical properties alter water and energy fluxes of an oak-grass savanna and an annual grassland. *Agric. For. Meteorol.* **2004**, *123*, 13–39. [\[CrossRef\]](#)
70. Ryu, Y.; Baldocchi, D.D.; Ma, S.; Hehn, T. Interannual variability of evapotranspiration and energy exchanges over an annual grassland in California. *J. Geophys. Res.* **2008**, *113*, D09104. [\[CrossRef\]](#)
71. Baldocchi, D.D.; Meyers, T.P. On using eco-physiological, micrometeorological and biogeochemical theory to evaluate carbon dioxide, water vapor and gaseous deposition fluxes over vegetation. *Agric. For. Meteorol.* **1998**, *90*, 1–25. [\[CrossRef\]](#)
72. Chen, B.; Black, T.A.; Coops, N.C.; Hilker, T.; Trofymow, J.A.; Morgenstern, K. Assessing Tower Flux Footprint Climatology and Scaling Between Remotely Sensed and Eddy Covariance Measurements. *Bound.-Lay. Meteorol.* **2009**, *130*, 137–167. [\[CrossRef\]](#)

73. Twine, T.E.; Kustas, W.P.; Norman, J.M.; Cook, D.R.; Houser, P.R.; Meyers, T.P.; Prueger, J.H.; Starks, P.J.; Wesely, M.L. Correcting eddy-covariance flux underestimates over a grassland. *Agric. For. Meteorol.* **2000**, *103*, 279–300. [[CrossRef](#)]
74. Wilson, K.; Goldstein, A.; Falge, E.; Aubinet, M.; Baldocchi, D.; Berbigier, P.; Bernhofer, C.; Ceulermans, R.; Dolman, H.; Field, C.; et al. Energy balance closure at FLUXNET sites. *Agric. For. Meteorol.* **2002**, *113*, 223–234. [[CrossRef](#)]
75. Chehbouni, A.; Hoedjes, J.C.B.; Rodriguez, J.-C.; Watts, C.J.; Garatuza, J.; Jacob, F.; Kerr, Y. Using remotely sensed data to estimate area-averaged daily surface fluxes over a semi-arid mixed agricultural land. *Agric. For. Meteorol.* **2008**, *148*, 330–342.
76. Baldocchi, D.D.; Ma, S. How will land use affect air temperature in the surface boundary layer? Lessons learned from a comparison study on the energy balance of an oak savanna and annual grassland in California, USA. *Tellus* **2013**, *65*, 19994. [[CrossRef](#)]
77. Foken, T. The energy balance closure problem: An overview. *Ecol. Appl.* **2008**, *18*, 1351–1367. [[CrossRef](#)]
78. Leuning, R.; Van Gorsel, E.; Massman, W.J.; Isaac, P.R. Reflections on the surface energy imbalance problem. *Agric. For. Meteorol.* **2012**, *156*, 65–74. [[CrossRef](#)]
79. Garrigues, S.; Olioso, A.; Calvet, J.-C.; Martin, E.; Lafont, S.; Moulin, S.; Chanzy, A.; Marloie, O.; Buis, S.; Desfonds, V.; et al. Evaluation of land surface model simulations of evapotranspiration over a 12-year crop succession: Impact of soil hydraulic and vegetation properties. *Hydrol. Earth Syst. Sci.* **2015**, *19*, 3109–3131. [[CrossRef](#)]
80. AmeriFlux. Available online: <http://ameriflux.ornl.gov> (accessed on 29 December 2018).
81. Boulet, G.; Mougnot, B.; Lhomme, J.-P.; Fanise, P.; Lili-Chabaane, Z.; Olioso, A.; Bahir, M.; Rivalland, V.; Jarlan, L.; Merlin, O.; et al. The SPARSE model for the prediction of water stress and evapotranspiration components from thermal infra-red data and its evaluation over irrigated and rainfed wheat. *Hydrol. Earth Syst. Sci.* **2015**, *19*, 4653–4672. Available online: [www.hydrol-earth-syst-sci.net/19/4653/2015/](http://www.hydrol-earth-syst-sci.net/19/4653/2015/) (accessed on 7 March 2019). [[CrossRef](#)]
82. Ghilain, N.; Arboleda, A.; Gellens-Meulenberghs, F. Evapotranspiration modelling at large scale using near-real time MSG SEVIRI derived data. *Hydrol. Earth Syst. Sci.* **2011**, *15*, 771–786. [[CrossRef](#)]
83. Roerink, G.J.; Su, Z.; Menenti, M. S-SEBI: A simple remote sensing algorithm to estimate the surface energy balance. *Phys. Chem. Earth. Pt B* **2000**, *25*, 147–157. [[CrossRef](#)]
84. Su, Z. The Surface Energy Balance System (SEBS) for estimation of turbulent heat fluxes. *Hydrol. Earth Syst. Sci.* **2002**, *6*, 85–100. [[CrossRef](#)]
85. Guillevic, P.C.; Göttsche, F.; Nickeson, J.; Hulley, G.; Ghent, D.; Yu, Y.; Trigo, I.; Hook, S.; Sobrino, J.A.; Remedios, J.; et al. Land Surface Temperature Product Validation Best Practice Protocol. Version 1.1. In *Best Practice for Satellite-Derived Land Product Validation*; Guillevic, P., Göttsche, F., Nickeson, J., Román, M., Eds.; Land Product Validation Subgroup (WGCV/CEOS), NASA Goddard Space Flight Center: Greenbelt, MD, USA, 2018; p. 58.
86. Guillevic, P.C.; Bork-Unkelbach, A.; Goettsche, F.M.; Hulley, G.; Gastellu-Etchegorry, J.P.; Olesen, F.; Privette, J.L. Directional viewing effects on Satellite Land Surface Temperature products over sparse vegetation canopies—A multi-sensor analysis. *IEEE Geosci. Remote Sens. Lett.* **2013**, *10*, 1464–1468. [[CrossRef](#)]
87. Kalma, J.D.; McVicar, T.R.; McCabe, M.F. Estimating Land Surface Evaporation: A Review of Methods Using Remotely Sensed Surface Temperature Data. *Surv. Geophys.* **2008**, *29*, 421–469. [[CrossRef](#)]
88. Petropoulos, G.; Carlson, T.N.; Wooster, M.J.; Islam, S. A review of Ts/VI remote sensing based methods for the retrieval of land surface energy fluxes and soil surface moisture. *Prog. Phys. Geogr.* **2009**, *33*, 224–250. [[CrossRef](#)]
89. Karimi, P.; Bastiaanssen, W.G.M. Spatial evapotranspiration, rainfall and land use data in water accounting—Part 1: Review of the accuracy of the remote sensing data. *Hydrol. Earth Syst. Sci.* **2015**, *19*, 507–532. [[CrossRef](#)]
90. Kustas, W.P.; Norman, J.M.; Anderson, M.C.; French, A.N. Estimating subpixel surface temperatures and energy fluxes from the vegetation index-radiometric temperature relationship. *Remote Sens. Environ.* **2003**, *85*, 429–440. [[CrossRef](#)]
91. Eswar, R.; Sekhar, M.; Bhattacharya, B.K.; Bandyopadhyay, S. Spatial Disaggregation of Latent Heat Flux Using Contextual Models over India. *Remote Sens.* **2017**, *9*, 949. [[CrossRef](#)]

92. Eswar, R.; Sekhar, M.; Bhattacharya, B.K. A simple model for spatial disaggregation of evaporative fraction: Comparative study with thermal sharpened land surface temperature data over India. *J. Geophys. Res. Atmos.* **2013**, *118*, 12029–12044. [[CrossRef](#)]
93. Cammalleri, C.; Anderson, M.C.; Gao, F.; Hain, C.R.; Kustas, W.P. Mapping daily evapotranspiration at field scales over rainfed and irrigated agricultural areas using remote sensing data fusion. *Agric. For. Meteorol.* **2014**, *186*, 1–11. [[CrossRef](#)]
94. Gao, F.; Masek, J.; Schwaller, M.; Hall, F.G. On the blending of the Landsat and MODIS surface reflectance: Predicting daily Landsat surface reflectance. *IEEE Trans. Geosci. Remote Sens.* **2006**, *44*, 2207–2218.
95. Bindhu, V.M.; Narasimhan, B.; Sudheer, K.P. Development and verification of a non-linear disaggregation method (NL-DisTrad) to downscale MODIS land surface temperature to the spatial scale of Landsat thermal data to estimate evapotranspiration. *Remote Sens. Environ.* **2013**, *135*, 118–129. [[CrossRef](#)]
96. Guillevic, P.C.; Privette, J.L.; Coudert, B.; Palecki, M.A.; Demarty, J.; Ottlé, C.; Augustine, J.A. Land Surface Temperature product validation using NOAA's surface climate observation networks—Scaling methodology for the Visible Infrared Imager Radiometer Suite (VIIRS). *Remote Sens. Environ.* **2012**, *124*, 282–298. [[CrossRef](#)]
97. Guillevic, P.C.; Biard, J.; Hulley, G.C.; Privette, J.L.; Hook, S.J.; Olios, A.; Götsche, F.-M.; Radocinski, R.; Román, M.O.; Yu, Y.; et al. Validation of Land Surface Temperature products derived from the Visible Infrared Imager Radiometer Suite (VIIRS) using ground-based and heritage satellite measurements. *Remote Sens. Environ.* **2014**, *154*, 19–37. [[CrossRef](#)]



© 2019 by the authors. Licensee MDPI, Basel, Switzerland. This article is an open access article distributed under the terms and conditions of the Creative Commons Attribution (CC BY) license (<http://creativecommons.org/licenses/by/4.0/>).